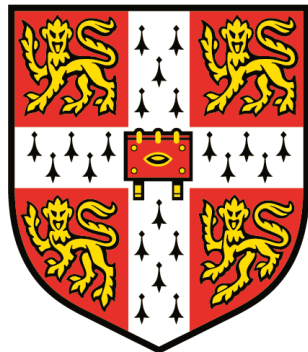


Quantifying melt rates in the grounding zones of Antarctic ice shelves



Reefe Conley

Department of Applied Mathematics and Theoretical Physics
University of Cambridge

This dissertation is submitted in partial fulfilment of the requirements of
Part III of the Natural Sciences Tripos

Word count: 9108

Girton College

July 2025

Declaration

This report is the result of my own work and includes nothing which is the outcome of work done in collaboration except as declared in the Preface and specified in the text. It is not substantially the same as any work that has already been submitted, or, is being concurrently submitted for any degree, diploma or other qualification at the University of Cambridge or any other University or similar institution except as declared in the preface and specified in the text. It does not exceed the prescribed word limit.

I also confirm that I have read and understood the Faculty of Mathematics Guidelines on Plagiarism and the University-wide Statement on Plagiarism.

Reefe Conley

A handwritten signature in black ink, appearing to read "R. Conley".

29th July, 2025

Abstract

Antarctic ice shelves in the Amundsen Sea embayment are vulnerable to rapid disintegration, the dynamics of which depend strongly on the rate of melting in the grounding zone, where floating ice contacts bedrock. It is therefore important to constrain melt rates in these regions. To do this, the ice shelf thickness must be determined in the grounding zone. The hydrostatic model is widely used for this purpose; however, this model fails in the grounding zone, where elastic flexure of ice causes significant deviations from hydrostatic equilibrium.

This dissertation proposes a novel inverse approach for inferring ice thickness in the grounding zones of Antarctic ice shelves by accounting for this elastic flexure. This ‘flexural model’ is first developed and applied to a synthetic case for which an analytical solution for the shelf profile exists. The model is then applied to a selection of vulnerable ice shelves across the West Antarctic Ice Sheet, and its performance is compared with that of the hydrostatic model.

Acknowledgements

My sincere thanks to Professor Jerome Neufeld, Doctor Paul Holland and Doctor Adam Butler for their committed supervision, support and enthusiasm throughout this project.

Thanks also to Zhenya Tumarkin for proof-reading the first draft of this dissertation and to William Royce for helping set the schematic figures in L^AT_EX.

Contents

Contents	2
1 Introduction	4
1.1 Methods of remote sensing of grounding zones	5
1.2 Melt rate	6
1.3 Objectives	7
2 Theory and Methods	8
2.1 Force balance	8
2.1.1 Flotation	8
2.1.2 Bed compression	9
2.1.3 Bending stresses	9
2.1.4 Full force balance	11
2.2 Numerical approach	12
2.3 Melt rate	14
2.4 Data	16

3 Results and Discussion	18
3.1 Analytical solution	18
3.2 Thwaites Glacier	21
3.2.1 Parameter fitting	21
3.2.2 Inversions with tuned parameters	24
3.3 Pine Island Glacier	32
3.4 Pope Glacier	32
3.5 Smith East Glacier	36
3.6 Smith West Glacier	41
3.7 Kohler Glacier	43
3.8 Average melt rates	46
4 Conclusions and future work	49
References	51

Chapter 1

Introduction

Global mean sea level (GMSL) is projected to rise by 0.6–5.4 m by 2300, depending on the emissions scenario considered (Oppenheimer et al., 2019, pg. 328). However, uncertainty in centennial GMSL rise is dominated by ice sheet contributions (Van De Wal et al., 2019). In particular, there is concern that the West Antarctic Ice Sheet (WAIS) may collapse in a warming climate. The WAIS is a marine-based ice sheet, primarily lying on retrograde (inland-sloping) bedrock. Moreover, warm Circumpolar Deep Water has nearly uninhibited access to ice shelves in the Amundsen and Bellingshausen seas, warming the shelf bottom waters to $\sim 1^{\circ}\text{C}$ (Thompson et al., 2018). Together, these environmental conditions render the WAIS particularly prone to poorly understood, self-amplifying processes that have the potential to cause widespread disintegration of the WAIS. As the WAIS contains enough ice to raise GMSL by ~ 3.4 m (Oppenheimer et al., 2019, pg. 347), it is crucial to accurately assess its current state and rate of ice loss.

As surface temperature in Antarctica rarely rise above -10°C , the ice sheet experiences minimal ice mass loss through surface melting. Instead, basal melting at ice shelves is the primary driver of ice mass loss (Pritchard et al., 2012), accounting for over 50% of mass loss in 48 (37 to 52) of the 71 ice shelves that unambiguously lost mass between 1997 and 2021 (Davison et al., 2023). Basal melting has the most influence on ice shelf dynamics when it occurs in the grounding zone, the transition zone between the grounded ice sheet and the floating ice shelf. This region plays an important role in controlling ice sheet dynamics, as it controls the flow rate of ice moving from the cryosphere into the ocean, and responds sensitively to ocean warming (Schoof, 2007). If the underlying bedrock of an ice sheet is retrograde, then melting of the ice sheet's marine-terminating front can cause the grounding line to retreat deeper under the ice sheet, increasing the thickness of the ice sheet above it. As outward ice flow depends on the height of the

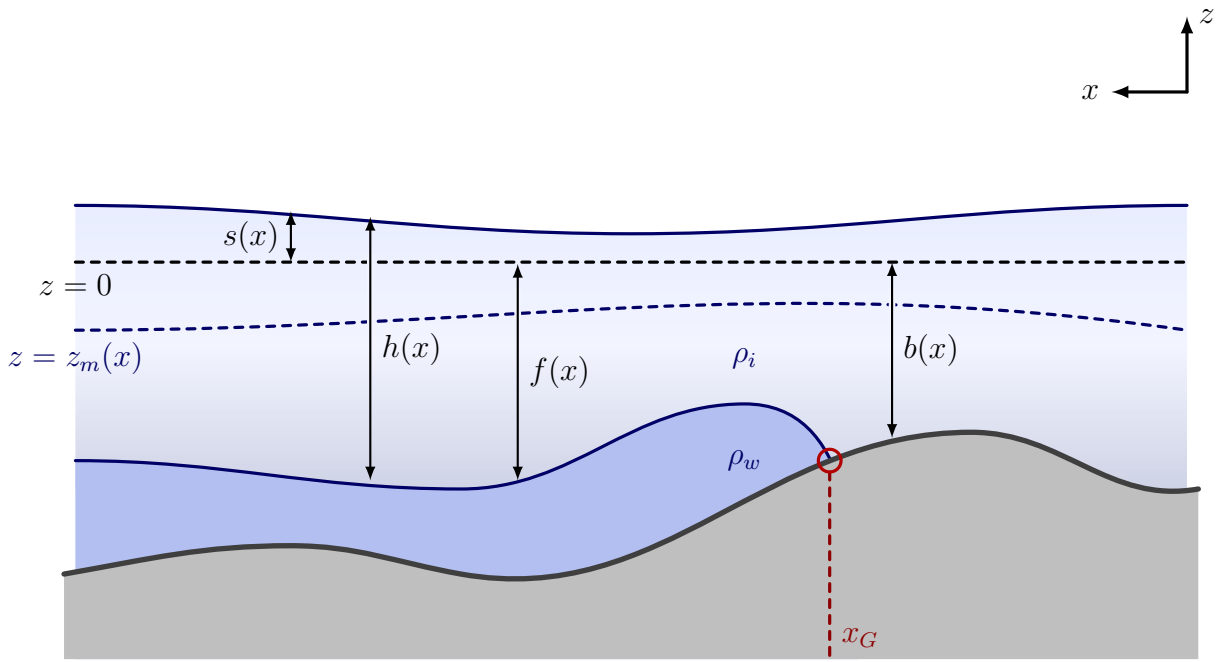


Figure 1.1: Schematic of a marine-terminating Antarctic glacier, with ice flowing from right to left. When ungrounded, the ice base may be approximated using the flotation condition. However, this approach interprets the elastic flexure of the ice sheet as a rapid melt and refreeze near the grounding line, x_G .

ice above the grounding line, any retreat of the marine-terminating front increases the outward flow of ice, thinning the ice sheet and causing more grounding line retreat. This self-reinforcing feedback is known as marine ice sheet instability (MISI; Weertman, 1974) and can break up previously-grounded ice sheets into floating ice masses, contributing to accelerating GMSL rise. The WAIS has the highest rates of basal melting and ice thinning in Antarctica (Davison et al., 2023; Rignot et al., 2013) and is particularly vulnerable to MISI, with glaciers such as Thwaites Glacier already thought to be unstable (Robel et al., 2019). Therefore, it is important to accurately locate the grounding zones and constrain the basal melting rates of ice sheets vulnerable to MISI.

1.1 Methods of remote sensing of grounding zones

Many remote sensing techniques are available for mapping Antarctic grounding zones. Broadly, they are split into dynamic and static methods (Friedl et al., 2020). Dynamic methods analyse the cm-scale flexure of ice shelves in response to tidal forcing, while static methods analyse the static flexure of ice shelves. Dynamic methods are most often performed with Differential SAR Interferometry (DInSAR) and can achieve a very high accuracy of ~ 100 m (Friedl et al., 2020). However, these methods require repeat pass

data to function, and the smallest current repeat pass interval is six days (Schmidt et al., 2018). This interval is often too long to maintain coherence in areas of fast ice flow and pronounced changes in surface elevation.

In contrast to the short time intervals required for dynamic methods, static methods analyse datasets compiled over multiple years. The simplest static method is the hydrostatic method, which estimates ice thickness using surface elevation data. Compiled datasets of ice surface elevation and bedrock height across Antarctica are freely available, and the hydrostatic model is computationally simple and efficient to implement at the continental scale (e.g. Rignot et al., 2013). Using Archimedes' principle, the hydrostatic ice bottom height $z = -f$ is given by

$$-f = s \frac{\rho_i}{\rho_i - \rho_w}, \quad (1.1)$$

where ρ_i and ρ_w are the densities of ice and seawater. The grounding line, or the transition point from grounded to ungrounded ice, is then the point at which the hydrostatic ice bottom height intersects with the bedrock. Far from the grounding line, ice is approximately in hydrostatic equilibrium, and the hydrostatic model provides a good approximation of ice thickness. However, close to the grounding line, elastic flexure causes the ice to be far from hydrostatic equilibrium, producing an apparent rapid melt and refreeze near the grounding line (Figure 1.1). Another limitation of the hydrostatic model for inferring grounding line position is its dependence on ρ_i and ρ_w . Antarctic-wide *in situ* measurements of ρ_i and ρ_w do not exist, so calculations are often performed with standard values of $\rho_i = 900 - 917 \text{ kg m}^{-3}$ and $\rho_w = 1024 - 1027 \text{ kg m}^{-3}$. Using different ice and water density values causes the inferred grounding line to shift position. Furthermore, the average density and depth of the firn layer across the grounding zone is often unknown, so these values are either assumed or ignored during the hydrostatic calculation. Together, changes in these assumptions can result in grounding line estimates of $\mathcal{O}(10 \text{ km})$, as shown in this dissertation. This effect is greatest in regions of low-sloping bedrock where ice shelf instabilities are most significant.

1.2 Melt rate

Direct *in situ* measurements of basal melt rates are expensive and spatially limited (Neckel et al., 2012). Therefore, remote sensing methods are widely applied to indirectly measure melt rates. The most accurate of these methods uses phase-sensitive radar to measure changes in thickness of an ice column (Corr et al., 2002). Although this method is highly

precise, it has only been applied to a few locations in Antarctica and requires a knowledge of the strain rate in the ice to account for the effect of strain thinning on ice thickness.

A simpler indirect method of determining basal melt rates uses an assumption of mass conservation in the ice shelf. Assuming an ice shelf is of uniform density, mass conservation is equivalent to volume conservation, which may be expressed as

$$\frac{\partial h}{\partial t} + \nabla \cdot (h\mathbf{u}) = a_s + a_b, \quad (1.2)$$

where $\nabla \cdot$ denotes horizontal divergence, h is ice thickness, $\mathbf{u} = (u, v)$ is depth-independent horizontal velocity, and a_s and a_b are surface and basal melt rates (Jenkins and Doake, 1991). In steady state, $\partial h / \partial t = 0$ and the horizontal divergence of the volume flux is exactly balanced by the sum of the surface and basal melt rates. Surface melt rates account for roughly 10–15 % of observed ice-shelf thinning in the Amundsen Sea embayment (Khazendar et al., 2016). Therefore, it is neglected, and all changes in ice thickness are assumed to be due to basal melting. The assumption of hydrostatic equilibrium has been widely used to infer basal melt rates in Antarctica (e.g. Rignot et al., 2013; Adusumilli et al., 2020; Depoorter et al., 2013). A limitation of this method is that it requires high-quality datasets of ice velocity, ice thickness and snow accumulation, as small uncertainties in the input data are more likely to dominate the residual mass flux (Neckel et al., 2012). Despite these limitations, this mass continuity approach is the method taken in this dissertation to measure basal melt rates, owing to its practicality and ease of application across ice shelves in comparison to other direct and indirect methods.

1.3 Objectives

The objectives of this research project are threefold: first, the elastic flexure of a floating ice shelf will be incorporated into the inversion process for its ice thickness; second, this improved ice thickness profile will be combined with surface ice velocity measurements to construct a melt rate profile across the shelf; finally, this method will be applied to a selection of ice shelves across Western Antarctica to assess their melt rates, stability, and future potential to contribute to GMSL rise.

Chapter 2

Theory and Methods

We model the ice sheet in two dimensions, as shown in Figure 1.1, where the x -coordinate increases leftward along the transect. We assume that the static shape and thickness of the ice is determined by the balance between its weight, the elastic bending stresses within the ice, and any normal stresses applied to the exterior of the ice. Where the ice is floating, the normal stresses are provided by buoyant forces, and where the ice is grounded, the normal stresses are provided by bed compression.

Dr Adam Butler provided a numerical framework for the numerical approach outlined in Section 2.1.4, written in MATLAB. This code was re-written in Python and substantially updated to improve model stability and speed of convergence, including the addition of the adaptive relaxation method and $\partial s_{\text{data}}/\partial x$ smoothing described in Section 2.1.4.

2.1 Force balance

2.1.1 Flotation

Floating ice is in hydrostatic equilibrium and obeys Archimedean balance,

$$\rho_i g h = \rho_w g f, \quad (2.1)$$

from which the ice midline, $z_m = s - h/2$, is given by

$$z_m = \left(\frac{1}{2} - \frac{\rho_i}{\rho_w} \right) h. \quad (2.2)$$

where h is the ice thickness (see Figure 1.1). Initial characteristic ice and seawater densities were taken as $\rho_i = 878.8 \text{ kg m}^{-3}$ and $\rho_w = 1000 \text{ kg m}^{-3}$.

2.1.2 Bed compression

Treating the bedrock as a Winkler foundation with spring constant k , then grounded ice purely supported by bed compression experiences a restoring force described by Hooke's Law,

$$\rho_i g h = k(f - b_0), \quad (2.3)$$

where $z = -b_0$ is the height of the uncompressed bedrock surface. From this, the ice midline, $z_m = -f + h/2$, is given by

$$z_m = -b_0 + \left(\frac{1}{2} - \frac{\rho_i g}{k} \right) h. \quad (2.4)$$

If the ice lies on the bedrock below the sea surface, it is supported by bed compression and buoyancy,

$$\rho_i g h = k(f - b_0) + \rho_w g f, \quad (2.5)$$

from which the ice midline is given by

$$z_m = \left[\frac{1}{2} - \frac{\left(\frac{\rho_i}{\rho_w} \right)}{1 + \left(\frac{k}{\rho_w g} \right)} \right] h - \left[\frac{\left(\frac{k}{\rho_w g} \right)}{1 + \left(\frac{k}{\rho_w g} \right)} \right] b_0. \quad (2.6)$$

2.1.3 Bending stresses

The bending behaviour of an elastic ice sheet may be modelled using the Euler-Bernoulli beam equation,

$$\frac{d^2}{dx^2} \left[B(x) \frac{d^2 z_m}{dx^2} \right] = p(x, z_m), \quad (2.7)$$

where $p(x, z_m)$ is the load on the sheet and $B(x)$ is the bending stiffness, given by

$$B(x) = \frac{E[h(x)]^3}{12(1 - \nu^2)}, \quad (2.8)$$

where E and ν are the Young's modulus and Poisson's ratio of the ice (Hetényi, 1946; Schmeltz et al., 2002; Sayag and Worster, 2011; Holdsworth, 1969). The elastic properties of the ice are assumed constant, so the spatial variation in bending stiffness is only a function of ice thickness.

Equation (2.7) represents a force balance between the bending stress in the ice and the distributed reaction force from either the bedrock or the ocean. For an ice sheet whose grounding line lies below the ocean surface, the force balance in the grounded and ungrounded regions is

$$\frac{d^2}{dx^2} \left(B \frac{d^2 z_m}{dx^2} \right) = \begin{cases} k \left(\frac{h}{2} - z_m - b_0 \right) - \rho_i g h & \text{if } x \leq x_g, \\ \rho_w g \left(\frac{h}{2} - z_m \right) - \rho_i g h & \text{if } x > x_g. \end{cases} \quad (2.9)$$

Scaling the bending and buoyancy terms in (2.9),

$$\frac{B z_m}{l^4} \sim \rho_w g z_m, \quad (2.10)$$

$$l \sim \left(\frac{B}{\rho_w g} \right)^{\frac{1}{4}}, \quad (2.11)$$

we obtain the characteristic bending-buoyancy length scale over which elastic flexure of the ice shelf occurs. Using a typical ice shelf thickness, Young's modulus and water density, we obtain a typical bending-buoyancy length scale of $l \sim 1$ km.

The applicability of elastic theory to an ice sheet/shelf depends on the magnitude of the bending stress at the grounding line. Laboratory experiments covering temperatures down to -50°C yield a stress range of less than 200 kPa for which elastic theory is applicable (Budd and Jacka, 1989). To determine whether elastic theory may be used to model ice shelf flexure, a scaling analysis was used to determine the characteristic magnitude of bending stresses in the grounding zone. Using characteristic ice values of $E \sim 10$ GPa and $\nu = 0.3$ (Gammon et al., 1983), along with conservative characteristic changes in ice thickness and midline position $\Delta h \sim 100$ m, $\Delta z_m \sim 10$ m across the grounding zone of width $l \sim 1$ km, a characteristic bending stress, σ_g , is given by

$$\sigma_g = \left. \frac{d^2}{dx^2} \left(B \frac{d^2 z_m}{dx^2} \right) \right|_{x_g} \sim \frac{E \Delta h^3 \Delta z_m}{12(1 - \nu^2) l^4} \sim 10 \text{ kPa}. \quad (2.12)$$

This value is well within the limits of elastic theory; therefore, it is reasonable to analyse grounding zone flexure using an elastic model. However, the bending stress is a strong function of Δh across the grounding zone. For a larger flexure, say $\Delta h \sim 200$ m, $\Delta z_m \sim 20$ m and $\sigma_g \sim 160$ kPa, we approach the limit of the applicability of elastic theory to model the flexure.

2.1.4 Full force balance

To determine the static shape and thickness of the ice, we combine the above forces into an overall force balance in terms of the ice thickness h and midline position z_m ,

$$\gamma \frac{d^2}{dx^2} \left(h^3 \frac{d^2 z_m}{dx^2} \right) + \rho_i g h = k \left(\frac{h}{2} - z_m - b_0 \right) \mathbb{1}(h/2 - z_m - b_0) + \rho_w g \left(\frac{h}{2} - z_m \right) \mathbb{1}(h/2 - z_m), \quad (2.13)$$

where the bending stress in the ice has been rewritten using

$$\frac{d^2}{dx^2} \left(B(x) \frac{d^2 z_m}{dx^2} \right) = \gamma \frac{d^2}{dx^2} \left([h(x)]^3 \frac{d^2 z_m}{dx^2} \right), \quad (2.14)$$

$$\gamma = \frac{E}{12(1 - \nu^2)}, \quad (2.15)$$

and $\mathbb{1}(x)$ is the unit step function, defined as

$$\mathbb{1}(x) = \begin{cases} 1 & \text{if } x \geq 0, \\ 0 & \text{if } x < 0. \end{cases} \quad (2.16)$$

The unit step functions apply the appropriate supporting forces when the ice is grounded, $\mathbb{1}(h/2 - z_m - b) = 1$, and/or below sea level, $\mathbb{1}(h/2 - z_m) = 1$.

Equation (2.13) is a fourth-order differential equation so requires four boundary conditions. To obtain these, we impose either pure flotation, (2.2), or pure bed compression, (2.4) or (2.6), at the last two grid cells on either end of the domain (Figure 2.1).

2.2 Numerical approach

Rearranging (2.13), we obtain

$$\gamma \frac{d^2}{dx^2} \left(h^3 \frac{d^2 z_m}{dx^2} \right) + \left[\left(\frac{k}{\rho_w g} \right) \mathbb{1}(h/2 - z_m - b_0) + \mathbb{1}(h/2 - z_m) \right] z_m = \left(\frac{k}{\rho_w g} \right) \left(\frac{h}{2} - b_0 \right) \mathbb{1}(h/2 - z_m - b_0) + \left(\frac{h}{2} \right) \mathbb{1}(h/2 - z_m) - \left(\frac{\rho_i}{\rho_w} \right) h. \quad (2.17)$$

This is a nonlinear equation, owing to the product of z_m with the unit step functions containing z_m . We use an iterative approach to solve this equation for $z_m(x)$, $h(x)$ and $b_0(x)$. First, we perform an ‘inner’ iteration to determine $z_m(x)$ for a given set of height and bedrock profiles, $h^{\text{init}}(x)$, $b_0^{\text{init}}(x)$. This applies the force balance in (2.13) using the prescribed height and bedrock profiles. The inner iteration proceeds by substituting an initial guess for the midline profile, $z_m^0(x)$, into the unit step functions in (2.17) and solving for an updated profile, z_m^{new} , which may then be used as a new initial guess. This process is repeated until the residual $|z_m^{\text{new}}(x) - z_m^0(x)|$ falls below a threshold value.

With a midline profile z_m satisfying the full force balance, we then perform an ‘outer’ iteration to determine $h(x)$ and $b(x)$. To do this, we compare the ice surface elevation $s(x)$ and bedrock topography $b(x)$ suggested by the inner iteration with the known surface and bedrock elevation data, $s_{\text{data}}(x)$, $b_{\text{data}}(x)$. To update our $h(x)$ and $b_0(x)$ profiles, we apply the Newton-Raphson method to minimise the errors $\epsilon_s = |s(x) - s_{\text{data}}(x)|^2$ and $\epsilon_b = |b(x) - b_{\text{data}}(x)|^2$. In this way, we iteratively approach a solution that satisfies both the force balance and the observed surface elevation and bedrock topography profiles, $s_{\text{data}}(x)$, $b_{\text{data}}(x)$.

The constants γ and $k/(\rho_w g)$ remain constant throughout the inversion process. To determine an appropriate γ value, we assume Poisson’s ratio of ice remains constant at 0.3. The Young’s modulus E and spring constant k are left as free parameters to be tuned using observational data (see Section 3.2.1). The Amundsen Sea water density ρ_w was initially set to an untuned value of 1000 kg m^{-3} but was later revised to 1027 kg m^{-3} to more closely align with consensus values reported in the literature (e.g. Mallett et al., 2018).

Figure 2.1 shows the initial $h^{\text{init}}(x)$, $b_0^{\text{init}}(x)$ and $z_m^{\text{init}}(x)$ profiles for each inversion. The initial ice thickness profile $h^{\text{init}}(x)$ is that of an ice shelf of uniform thickness

$$\frac{\rho_w}{\rho_w - \rho_i} s_{\text{data}}(x_f), \quad (2.18)$$

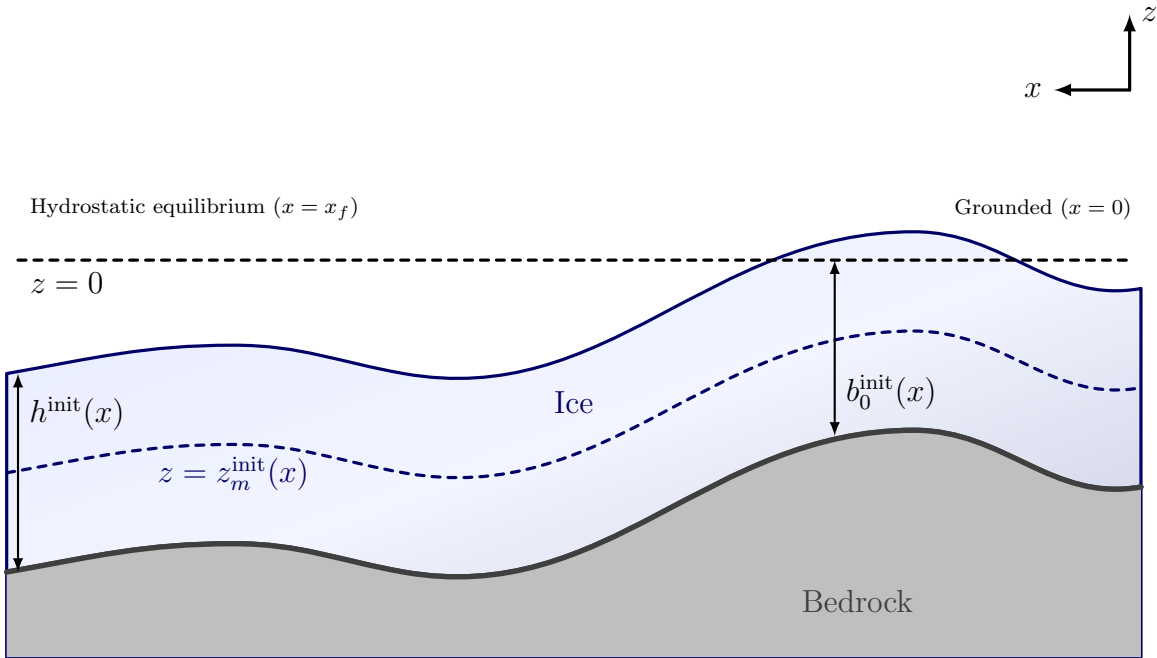


Figure 2.1: The initial ice shelf profile guess for each inversion. The ice is of uniform thickness equal to the hydrostatic thickness calculated at the leftmost end of the domain, x_f , and lies along the bedrock.

where x_f is the leftmost end of the domain, at which point ice is assumed to be in hydrostatic equilibrium. The initial guess for the uncompressed bed topography $b_0(x)$ is the observed compressed topography $b(x)$, and the initial $z_m(x)$ guess is prescribed by setting the initial ice shelf profile to be resting on the bedrock across the entire domain (Figure 2.1). Although this initial ice shelf guess violates the pure flotation (hydrostatic equilibrium) boundary condition on the left-hand side of the domain, this condition is enforced in all subsequent iterations.

A tempered relaxation method was implemented to ensure that these iterative processes approached their solutions stably. For a given parameter y updated by an iterative process, the tempered relaxation is of the form

$$y_{\text{new}} = y_{\text{old}} + \omega(y_{\text{update}} - y_{\text{old}}), \quad (2.19)$$

where $y_{\text{update}} - y_{\text{old}}$ is the change in y suggested by the iterative process and $0 \leq \omega \leq 1$ is a relaxation parameter. Therefore, only a fraction of the suggested step size is taken in each iteration; while this increases the number of iterations needed to converge to a sufficiently accurate solution, it removes some unstable behaviour associated with the iterative procedure. The outer iteration was found to be more sensitive to the step size than the inner iteration. The inner iteration relaxation parameter was fixed at $\omega_{\text{inner}} = 1$. Using smaller ω_{outer} values produced more stable inversions yet increased the time taken

for the model to converge to a solution. To improve model convergence while retaining some model speed, an adaptive relaxation method was implemented in which ω_{outer} varied with the size of the error ϵ_s . The initial value of ω_{outer} was selected based on the observed stability of the inversion process at each ice shelf. A value as low as $\omega_{\text{outer}} = 10^{-4}$ was used at the start of the inversion process and increased to $\omega_{\text{outer}} = 0.1$ as the error value decreased. This is because the Newton-Raphson method takes progressively smaller steps as the model error approaches zero. This adaptive approach ensures that the Newton-Raphson method does not overshoot a root when ϵ_s (and hence the suggested step size) is large, yet ensures the method converges to a root quickly when the error is close to zero (i.e. when there is little risk of overshooting).

The stability of the model was found to be sensitive to the surface data at the left-hand (floating) side of the domain. To improve model stability, $\partial s_{\text{data}}/\partial x$ was forced to zero at the floating boundary by smoothing the ice surface elevation data over the bending-buoyancy length scale before inversion. This significantly improved the stability of the model inversions without affecting the profile at the grounding zone. This approach is justified by the flexibility in transect length used for model inversions, which allows transects to be extended slightly beyond the region of interest, providing a ‘buffer zone’ for smoothing.

2.3 Melt rate

To determine the melt rate $a(x)$, we use mass conservation in the ice sheet/shelf,

$$\frac{\partial h}{\partial t} + \frac{\partial q}{\partial x} = a, \quad (2.20)$$

where h is ice thickness, q is the depth-integrated ice flux per unit width and a is the melt rate. In steady state, $\partial h/\partial t = 0$, leaving

$$\frac{\partial q}{\partial x} = a. \quad (2.21)$$

The ice flux per unit width is given by

$$q(x) = \int_{z_m - \frac{h}{2}}^{z_m + \frac{h}{2}} u(x, z) dz, \quad (2.22)$$

where $u(x, z)$ is the horizontal ice velocity in the direction of the ice sheet/shelf transect. The horizontal surface velocity $\mathbf{u}(x, z_m + h/2)$ field is known from satellite optical imagery.

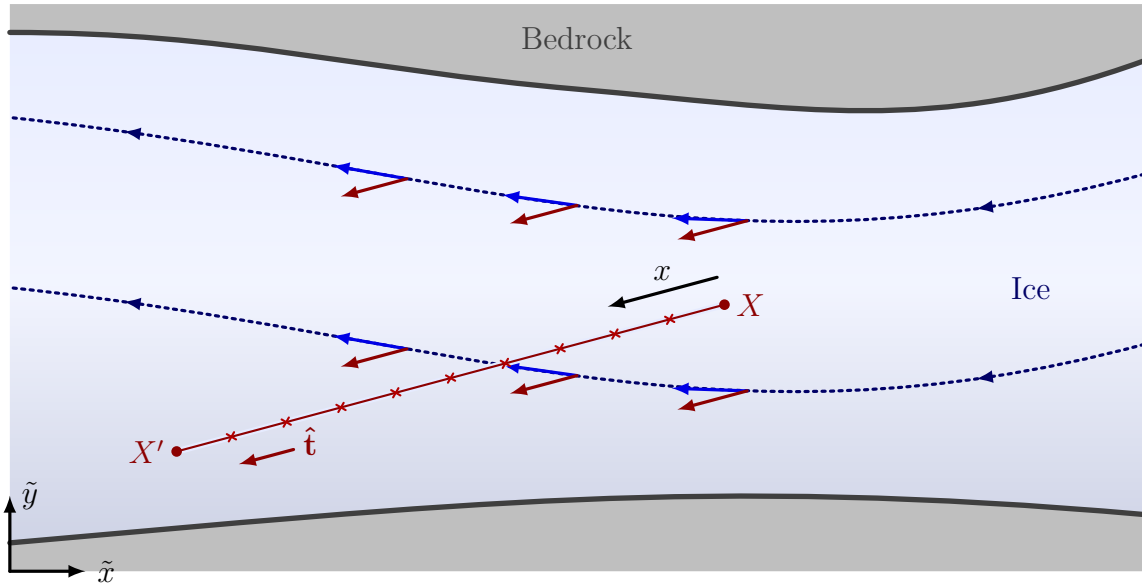


Figure 2.2: Plan view of a schematic ice stream illustrating the projection of horizontal surface ice velocities \mathbf{u} (blue vectors) onto the unit transect vector $\hat{\mathbf{t}}$. The projected velocity field (red vectors) is sampled at discrete points along the transect XX' (crosses). The x -coordinate increases along the transect and does not necessarily align with the easting (\tilde{x}) or northing (\tilde{y}) directions.

We calculate $u(x, z_m + h/2)$ along the transect using

$$u(x, z_m + h/2) = \mathbf{u}(x, z_m + h/2) \cdot \hat{\mathbf{t}}, \quad (2.23)$$

where $\hat{\mathbf{t}}$ is a unit vector in the direction of the transect increasing with the direction of ice flow; $u(x, z_m + h/2)$ is therefore the component of the horizontal surface velocity $\mathbf{u}(x, z_m + h/2)$ in the direction of the transect (Figure 2.2). Projecting the horizontal surface velocity field onto the transect direction ensures that no ice mass is transferred perpendicular to the transect plane. As a result, equation (2.21) is always satisfied, and any observed steady-state gradients in q can be attributed solely to melting or freezing.

To determine the melt rate along the ice sheet, we must calculate the ice flux $q(x)$. From equation (2.22), we require both the ice thickness h and horizontal velocity profile with depth in the ice column, $u(x, z)$, at each point along the transect to calculate $q(x)$. While an estimate for ice thickness is obtained through inversion, determining $u(x, z)$ requires assuming a relationship between the observed surface velocity and the horizontal velocity profile through the ice column.

The relationship between the observed surface velocity and the velocity profile within the ice column depends on the rheology of ice and on the boundary conditions imposed at the upper and lower boundaries of the ice. A commonly used rheological model is Glen's

flow law, which treats ice as a shear-thinning fluid,

$$\tau_{ij} = \mu \dot{\varepsilon}_{ij}, \text{ where} \quad (2.24)$$

$$\mu = A(T) \left| \frac{\partial u}{\partial z} \right|^{\frac{1}{n}-1} \quad (2.25)$$

is the effective ice viscosity, τ_{ij} is the stress tensor, $\dot{\varepsilon}_{ij}$ is the strain rate tensor, $A(0^\circ\text{C}) \approx 2.4 \times 10^{-24} \text{ Pa}^{-3} \text{ s}^{-1}$ is a rate factor (LeB. Hooke, 1981), and $n \approx 3$.

The marine ice shelf is assumed to have free-slip boundaries on both its upper and lower surfaces, producing a uniform horizontal velocity ('plug flow') throughout the ice sheet, removing the z -dependence of the horizontal ice velocity. The depth-integrated ice flux per unit width in the ice shelf is therefore

$$q(x) = u(x, z_m + h/2)h(x). \quad (2.26)$$

In contrast to the marine ice shelf, the grounded ice sheet only has a free-slip boundary on its upper surface. Assuming the ice surface is a free-slip boundary moving at observed speed $u(x, z_m + h/2)$ in the direction of the transect, Glen's flow law predicts (in the grounded ice sheet) a horizontal velocity profile

$$u(x, z) = \left(\frac{\rho g}{A} \frac{\partial h}{\partial x} \right)^3 \left[\frac{(z - z_m - \frac{h}{2})^4 - h^4}{4} \right] + u(x, z_m + h/2). \quad (2.27)$$

Although grounded ice typically follows a Glen's flow law velocity profile, a plug flow velocity profile was applied to both grounded and ungrounded regions. This choice was made because neither Glen's flow law nor a Newtonian rheology was suitable for calculating melt rates, owing to numerical inaccuracies in the calculation of $\partial h / \partial x$ in both cases. This assumption is justified given that little of the ice considered is grounded and the melt rates of interest primarily occur in the ungrounded regions.

2.4 Data

Ice surface elevation and bed topography data were obtained from the MEaSURES BedMachine Antarctica V3 ('BedMachine') dataset (Morlighem, 2022; Morlighem et al., 2020). These data are at 500 m resolution across all of Antarctica and are a composite of data collected between 1970 and 2019.

Ice surface elevation and ice base data were obtained from the IceBridge MCoRDS L2 Ice Thickness V1 ('radio-echo') dataset (Paden et al., [2010](#), updated 2019). These data consist of individual radio-echo transects with varying spatial resolution from 2009 to 2019. Transects were taken along radio-echo flight lines that aligned closest with the local direction of ice flow. This allowed comparison of the flexural model inversions with radio-echo observations along the same transect. Owing to this restriction, some transects were slightly mis-aligned with the local ice flow direction (notably in Smith East Glacier). This dataset has no associated uncertainty, although its spatial resolution is 10 m.

Ice velocity data were generated using auto-RIFT (Gardner et al., [2018](#)) and provided by the NASA MEaSUREs ITS_LIVE project (Gardner et al., [2022](#)).

Chapter 3

Results and Discussion

To verify the validity of this approach, inversions for $z_m(x)$, $h(x)$ and $b_0(x)$ were compared with the analytical solution given by Sayag and Worster (2011, eqs. 17 and 18) for the deflection profile of a long elastic sheet of uniform thickness resting on a sloping bed that is partially immersed in an ocean of higher density than the sheet. The model parameters were then fitted using observations from Thwaites Glacier to tune the model performance for application to real Antarctic ice shelves. Once tuned, the model was applied to the Pine Island, Pope, Smith and Kohler glaciers (Figure 3.1). These glaciers have undergone rapid thinning and retreat over the past three decades (Rignot et al., 2014; Milillo et al., 2019; Lilien et al., 2019), with the ice flux across the grounding zone of the combined Thwaites-Pope-Smith-Kohler glacier complex increasing by 10–15 Gt yr⁻¹ since 2009 (Mouginot et al., 2014; Martín-Español et al., 2016; Gardner et al., 2018).

3.1 Analytical solution

Figure 3.2 shows the deflection profile of an inversion for $z_m(x)$, $h(x)$ and $b_0(x)$ compared with the analytical solution. The inversion agrees closely with the analytical solution, with the inverted thickness deviating from the true beam thickness by a maximum of 3 % in the grounding zone. The flexural model grounding line is approximately 0.4 bending-buoyancy lengths from the true (analytical) grounding line.

Although the analytical solution is slightly more accurate than the flexural model, it is only applicable for a bed of constant slope and a beam of known uniform thickness and is

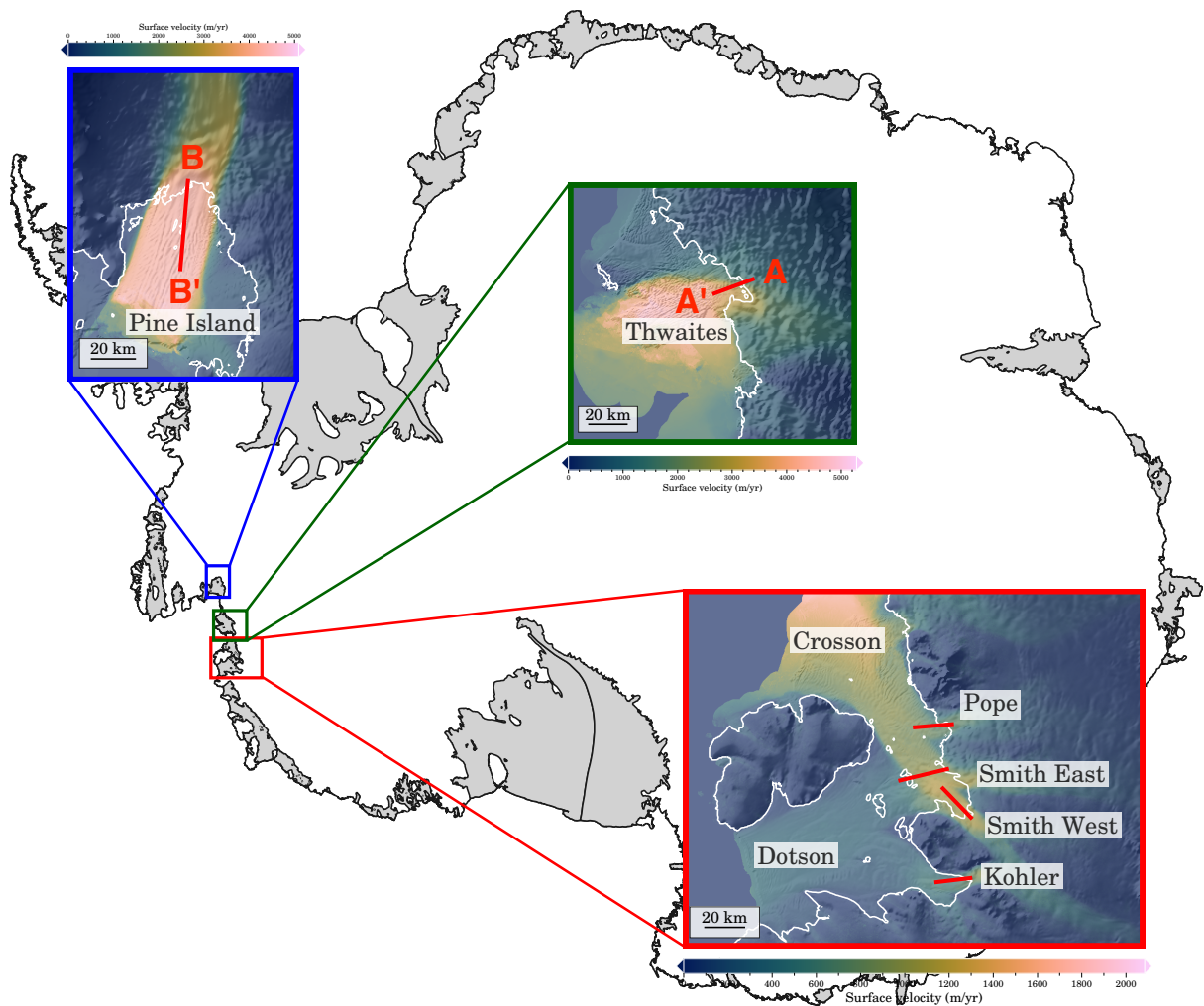


Figure 3.1: Map of Antarctica (Mouginot et al., 2017), showing the six ice shelves considered in this dissertation. Surface velocities are plotted over BedMachine surface elevation data. The hydrostatic grounding line (using $\rho_i = 917 \text{ kg m}^{-3}$ and $\rho_w = 1027 \text{ kg m}^{-3}$) is shown in white. Figure 3.13 shows the transect labels for the glaciers feeding the Crosson and Dotson ice shelves.

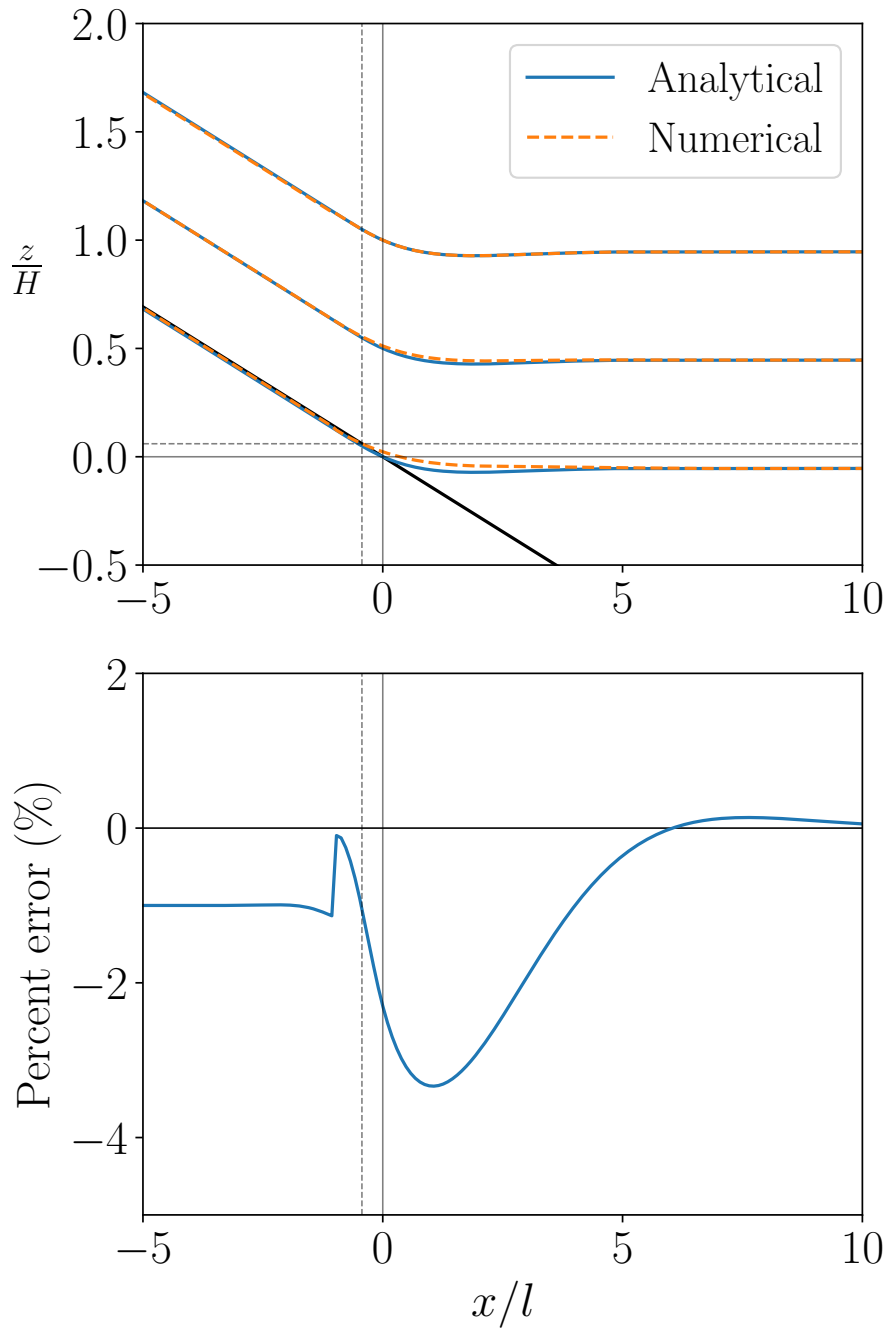


Figure 3.2: Top: Inversion for $z_m(x)$, $h(x)$ and $b_0(x)$ on a 3° bed. The numerical deflection profile (orange) agrees closely with the analytical profile (blue) given by Sayag and Worster (2011). Bottom: Percent error between the inverted $h(x)$ and known uniform beam thickness H . Analytical (solid) and numerical (dashed) grounding line positions and heights are shown in grey.

not widely applicable to the complex bed geometries and varying ice thicknesses observed in Antarctic grounding zones. The flexure model's close agreement to the analytical solution confirms its ability to accurately represent the effects of flotation, bending stresses and bed compression on the steady shape of the ice shelf. Moreover, the flexural model allows the ice thickness to vary across the ice sheet and applies a force balance at each point along the domain; therefore, it can produce ice sheet inversions of varying ice thicknesses across complex bed geometries for which analytical deflection profile solutions do not exist, making it widely applicable across Antarctica.

3.2 Thwaites Glacier

3.2.1 Parameter fitting

To fit the model parameters E and k , inversions for $z_m(x)$, $h(x)$ and $b_0(x)$ were compared with observed ice thickness data in the grounding zone of the Thwaites glacier. Figure 3.3 shows a set of model inversions through the Thwaites transect AA' (Figure 3.1) using a range of E and k values. The value of k was set by prescribing the value of the dimensionless ratio $k/\rho_i g$, after (Sayag and Worster, 2011). The range of E values were taken from Warburton et al. (2020), and the range of $k/\rho_i g$ values were taken from Sayag and Worster (2011), with $k/\rho_i g = 10^2$ taken as the characteristic stiffness of a soft bed and $k/\rho_i g = 10^8$ taken as the hard bed limit. Constant, untuned ice and water densities of $\rho_i = 878.8 \text{ kg m}^{-3}$ and $\rho_w = 1000 \text{ kg m}^{-3}$ were used throughout.

Close to the grounding line, the flexural model accounted for the flexure of the ice sheet, removing the apparent rapid melt and refreeze. Varying E and k did not change the flexural model grounding line position, confirming that the model is robust to variations in these parameters. The profiles using different values of $k/\rho_i g$ appear indistinguishable in Figure 3.3. To determine the effect that varying k had on the resulting profiles, the profile thicknesses h were compared between model runs using $k/\rho_i g = 10^2$ and $k/\rho_i g = 10^8$ (Figure 3.4). Changing the value of k caused changes in ice thickness of $\mathcal{O}(1 \text{ m})$. As this is smaller than the uncertainty of the satellite altimetry measurements and of the roughness of the undersides of Antarctic ice shelves, varying k is assumed to have no significant effect on model inversions, and a standard value of $k/\rho_i g = 10^5$ is assumed throughout this dissertation. The remaining free parameters that affect the model profile are therefore ρ_i , ρ_w and E . The values of these parameters were empirically determined by fitting a model inversion to an observed ice shelf profile along Thwaites

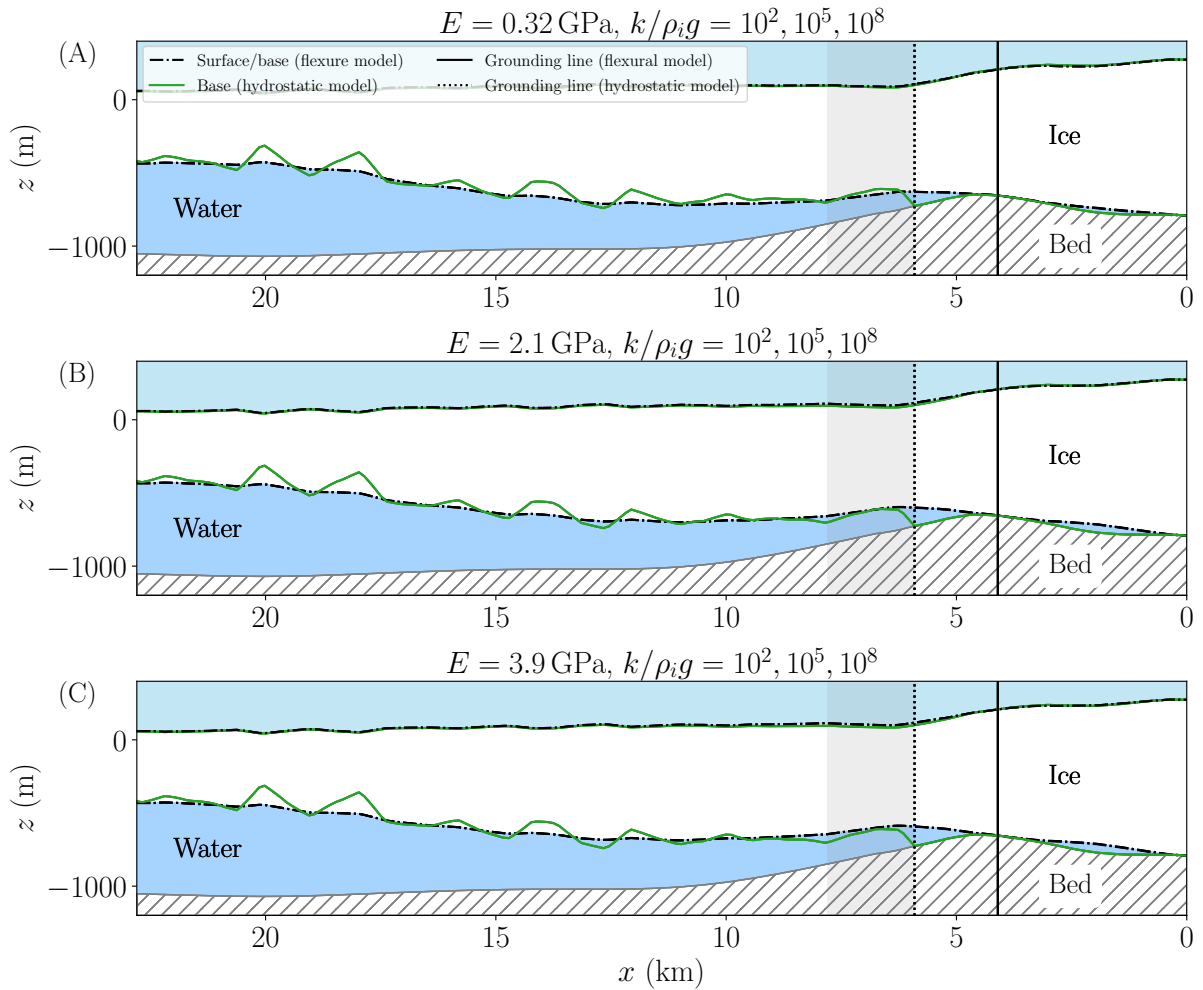


Figure 3.3: Best-fit ice shelf profiles for a range of E and k values through the Thwaites transect AA' . Ice flow is right to left. The value of E increases downwards. For each value of E , profiles using different values of $k/\rho_i g$ are plotted on the same plot, and are almost identical to one another. Grey shading shows region over which hydrostatic model interprets elastic flexure of ice sheet as a rapid melt and refreeze close to the grounding line.

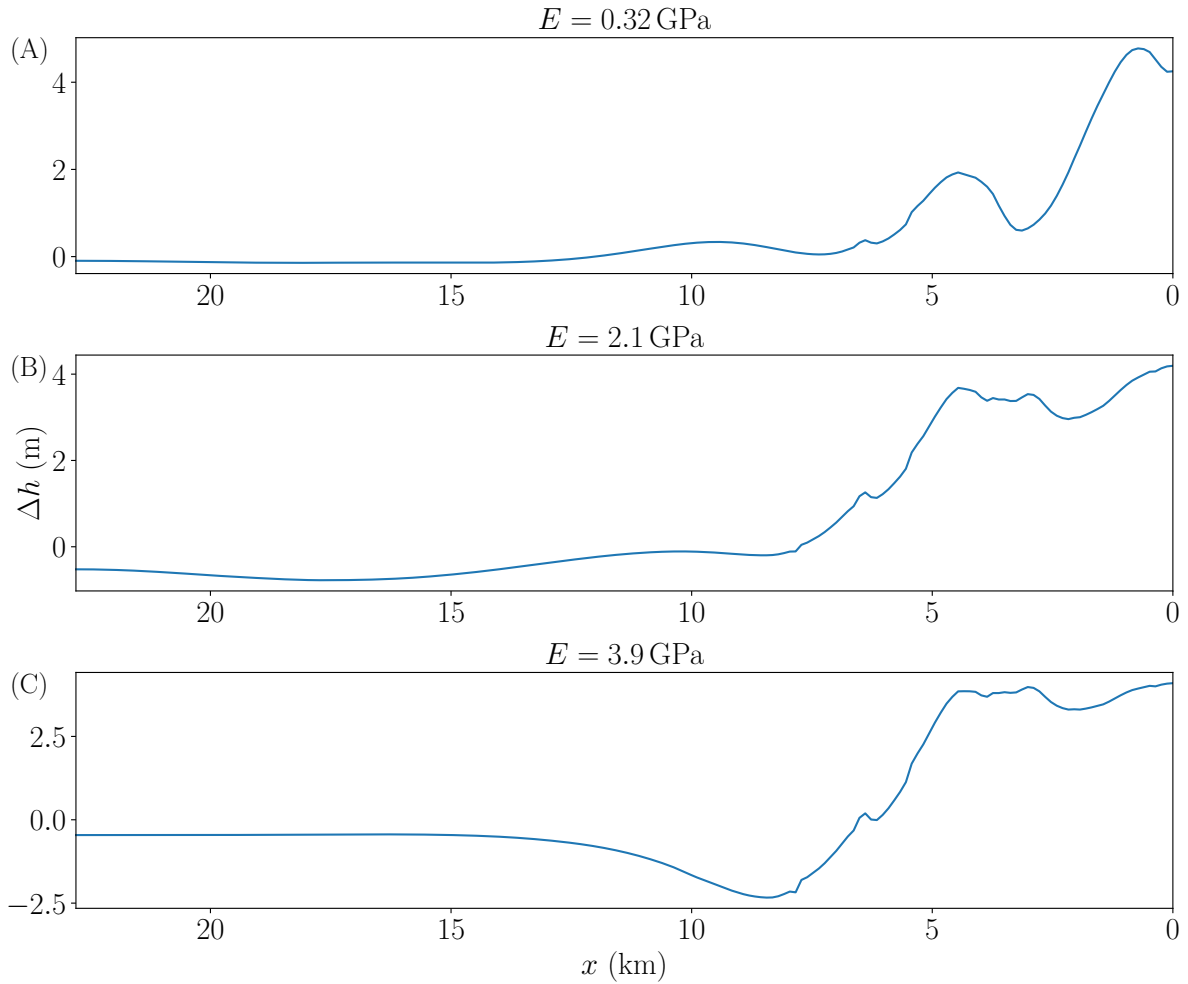


Figure 3.4: Change in ice thickness, h , between model runs with $k/\rho_i g = 10^2$ and $k/\rho_i g = 10^8$ ($\Delta h = h_{10^2} - h_{10^8}$) as a function of distance x along the AA' Thwaites transect. The value of E increases downwards.

Glacier.

Of the three model parameters ρ_w , ρ_i and E , we determine ρ_i from the observed ice thickness far from the grounding zone, where the ice is close to hydrostatic equilibrium. In this region, the value of E has no influence on the ice thickness. Instead, the hydrostatic thickness of ice of a given surface elevation depends only on the ratio ρ_i/ρ_w . Therefore, while the influence of E is eliminated, the problem of inferring ρ_w and ρ_i from a single far-field thickness remains underdetermined. To proceed, we must prescribe one of the densities and leave the other free to be fitted. In this dissertation, we prescribe the density of water and leave the density of ice to be fitted, as the water density in the Amundsen Sea embayment is relatively constant at $\sim 1027 \text{ kg m}^{-3}$ (Mallett et al., 2018). In contrast, the bulk density of an ice sheet can vary significantly, owing to effects such as degree of compaction, depth of firn layer, distribution of crevasses and other defects/impurities. Using the far-field ice thickness in this way allows a unique set of model parameters to be

determined for Thwaites Glacier. For other glaciers, we use the local far-field ice thickness to fit ρ_i specific to each glacier, while retaining the value of E fitted at Thwaites, based on the assumption that the ice shelves of interest have comparable elastic properties.

3.2.2 Inversions with tuned parameters

Figure 3.5A shows the Thwaites ice sheet along the transect AA' measured by radio-echo sounding. The resulting ice thickness h (Figure 3.5B) is used to calculate ρ_i along the transect using equation (2.1), assuming the ice is in hydrostatic equilibrium. Figure 3.5C shows the resulting ρ_i estimates along the Thwaites ice sheet using $\rho_w = 1000 \text{ kg m}^{-3}$ and $\rho_w = 1027 \text{ kg m}^{-3}$. Close to the grounding zone ($x/l \sim 1$), the ice is far from hydrostatic equilibrium, and the ρ_i estimate is unrealistically low. However, far from the grounding zone ($x/l \gg 1$), the inferred ice density reaches a value in line with typical ice density estimates of $\rho_i \approx 0.9\rho_w$.

If ρ_w is taken to be 1000 kg m^{-3} , then the resulting inferred ρ_i is consistent with a standard glacial $\rho_i = 917 \text{ kg m}^{-3}$. If a more typical Amundsen Sea water density of $\rho_w = 1027 \text{ kg m}^{-3}$ is used, the observed ice thickness is instead consistent with $\rho_i = 945 \text{ kg m}^{-3}$. This density is significantly higher than that of glacial ice, which is typically taken to be 917 kg m^{-3} . This discrepancy may be partially accounted for by the presence of 1027 kg m^{-3} water in the pore space of the ice sheet, increasing its mean density. An ice shelf porosity of 25 % is required to give a mean shelf density $\bar{\rho} = 945 \text{ kg m}^{-3}$ if solid ρ_i taken to be 917 kg m^{-3} and ρ_w is taken to be 1027 kg m^{-3} . This porosity is typical of the firn layer in the upper $\sim 100 \text{ m}$ of the ice shelf, but is unrealistic for the entire shelf. Despite being slightly unphysical, the higher shelf density of $\rho_i = 945 \text{ kg m}^{-3}$ was adopted for consistency with a water density of 1027 kg m^{-3} . This elevated density is specific to Thwaites Glacier; inferred densities for other ice shelves are generally closer to typical values for glacial ice.

To tune the effective Young's modulus value for use in the model, inversions were made within the range $0.5 \leq E \leq 3.2 \text{ GPa}$ and the root mean square error (RMSE) was calculated between the resulting modelled ice base and radar-derived measured ice base in the bending zone of Thwaites Glacier. The region $0 \leq x \leq 2l$ from the grounding line was used as the bending zone, with two bending-buoyancy length scales used to ensure a sufficient number of points for the error calculation. The results are shown in Figure 3.6 and suggest a tuned E value of 1.6 GPa . The range of E values for which the increase in RMSE above its minimum value was less than 1 m is taken as an estimate of the error of

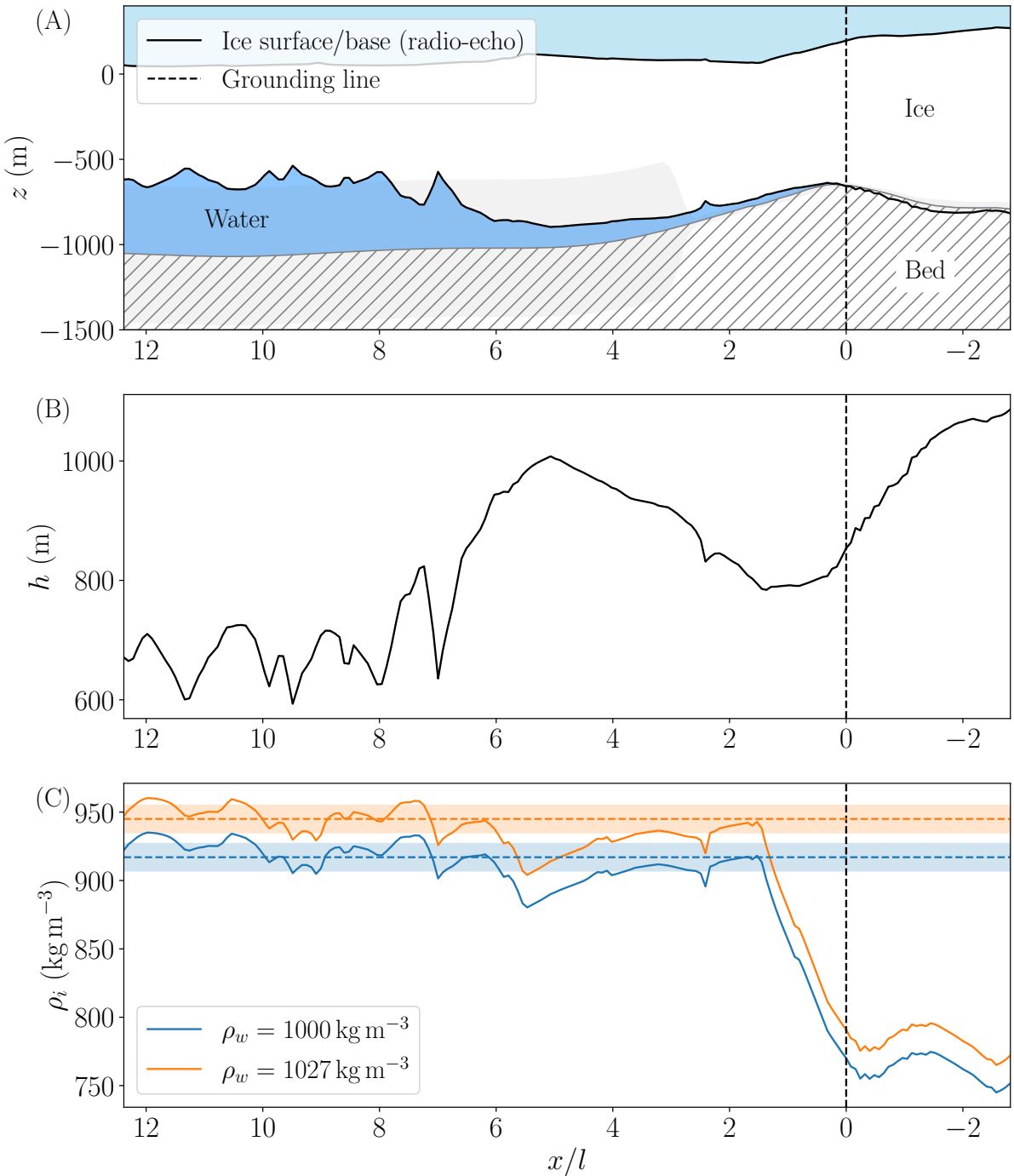


Figure 3.5: Transect AA' : (A) Thwaites ice shelf profile measured by radio-echo sounding. (B) Ice thickness profile along Thwaites ice shelf (using radio-echo data). (C) Hydrostatically inferred ice density ρ_i . All data are shown as a function of transect distance x from the grounding line in units of the bending-buoyancy length scale l . Shaded regions are $\pm 10 \text{ kg m}^{-3}$, after Dryak and Enderlin (2020). Ice flow is left-to-right.

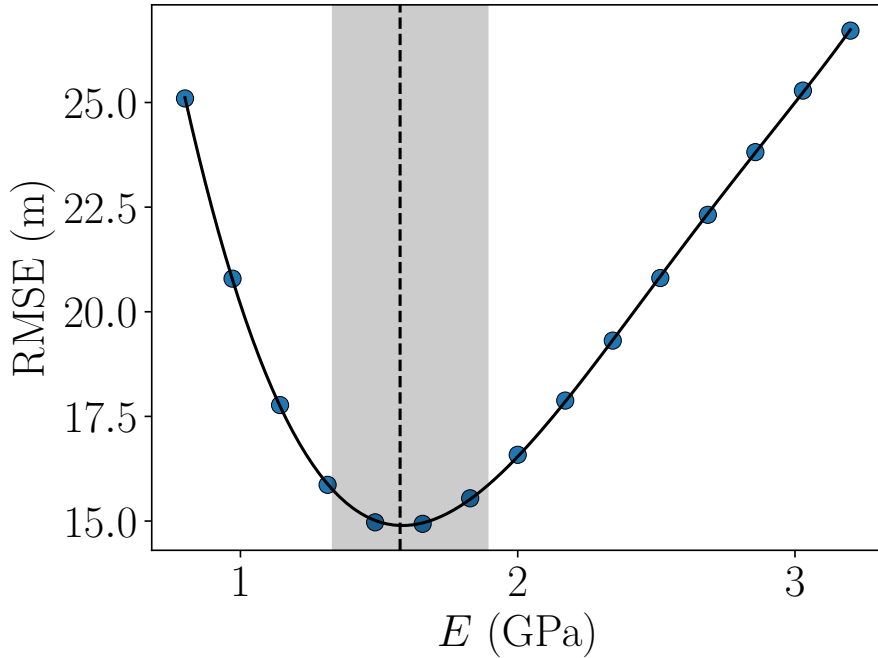


Figure 3.6: RMSE between the predicted and measured ice base in the region $0 \leq x \leq 2l$ as a function of E . The RMSE minimum is at approximately $E = 1.6$ GPa. The grey shading shows the range of E values for which the increase in RMSE above its minimum value is less than 1 m.

this fitted parameter, and gives an error range of approximately ± 0.2 GPa.

Laboratory measurements have found the Young's modulus of polycrystalline ice to be about 9 GPa (Schulson, 1999; Gammon et al., 1983). However, ice is not purely elastic, so direct comparisons cannot be made between laboratory measurements of ice elasticity and those derived from fitting tidal flexure profiles. Instead, ice is viscoelastic, and over long times significant strain can accumulate in natural ice masses, deforming the ice crystal fabric and causing an overall softening of the ice (Rosier et al., 2017). The lower field measurements of the Young's moduli of bulk ice masses are therefore only ‘effective’ moduli produced by fitting the observed deflection to a purely elastic plate model. Furthermore, it is likely that ice sheets contain more impurities, defects and anisotropic fabrics such as crystallographic preferred orientation than laboratory polycrystalline ice. These effects likely lower the Young's modulus of ice, causing further discrepancy between laboratory and field measurements.

Figure 3.7 shows inversions for a Thwaites glacier profile along the transect AA' using the tuned model parameters $\rho_i = 945 \text{ kg m}^{-3}$, $\rho_w = 1027 \text{ kg m}^{-3}$, $E = 1.6$ GPa and $k/\rho_i g = 10^5$. Separate inversions were performed using radio-echo (Figure 3.7B) and BedMachine (Figure 3.7C) surface elevation data. With these tuned ρ_i and E values, the inversion using radio-echo surface elevation data produced a good fit to the ice base observed by radio-echo sounding (lower red line, Figure 3.7B), and the resulting ice thickness

Thwaites Glacier

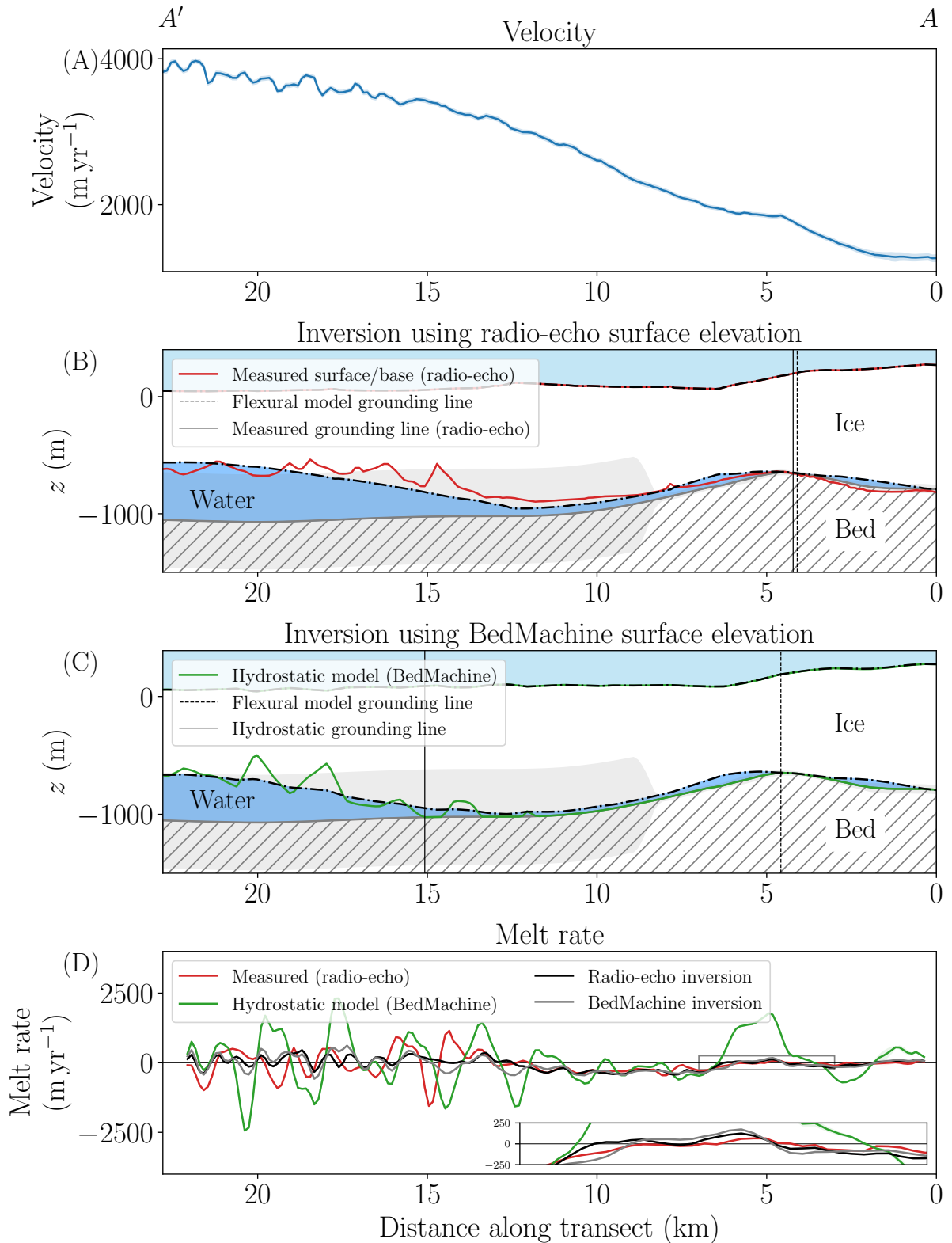


Figure 3.7: (A) Surface velocity in the direction of the transect AA' (B) Inversion for ice shelf profile using radio-echo surface elevation. (C) Inversion for ice shelf profile using BedMachine surface elevation. (D) Melt rate along the transect. Inversions used $\rho_i = 945 \text{ kg m}^{-3}$, $\rho_w = 1027 \text{ kg m}^{-3}$, $E = 1.6 \text{ GPa}$ and $k/\rho_i g = 10^5$. Ice flow is right to left.

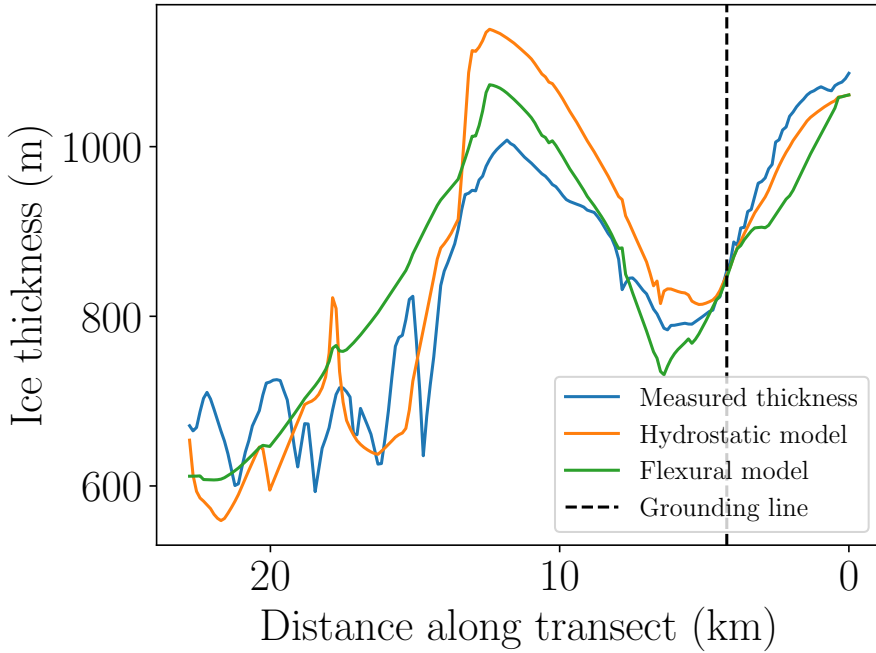


Figure 3.8: Ice thickness profile along Thwaites transect AA' . The hydrostatic model overestimates ice thickness, particularly in grounding zone where significant elastic flexure occurs. Note, only the radio-echo inversion results are shown here.

in the grounding zone aligns more closely to that measured by radio-echo sounding than predicted by the hydrostatic model (Figure 3.8). The inversion using BedMachine surface elevation data produced a similar shelf profile (Figure 3.7C). Both inversions predicted a grounding line position significantly closer to that measured by radio-echo sounding than to that predicted by the hydrostatic model (lower green line, Figure 3.7C). Moreover, there was close agreement in grounding line position between inversions using radio-echo and BedMachine surface elevation data.

To determine the sensitivity of the modelled grounding line position to variations in ice density, a sensitivity analysis was performed in which the model was run with a range of ice density values, and the resulting grounding line positions were compared to the observed position from radio-echo sounding (Figure 3.9). The flexural model grounding line position is significantly more robust to variations in ice density than the hydrostatic model.

The BedMachine bed height uncertainty is large over the ice shelf because the BedMachine bed height is calculated by subtracting an estimate of the ice thickness from the REMA surface elevation dataset (Howat et al., 2019), and it is over ice sheets where ice thickness estimates are the most poorly constrained. Despite this error range intersecting with the measured ice base, the radio-echo data do not indicate that the topography makes contact with the ice base in this region. In the grounded region, the radio-echo-derived

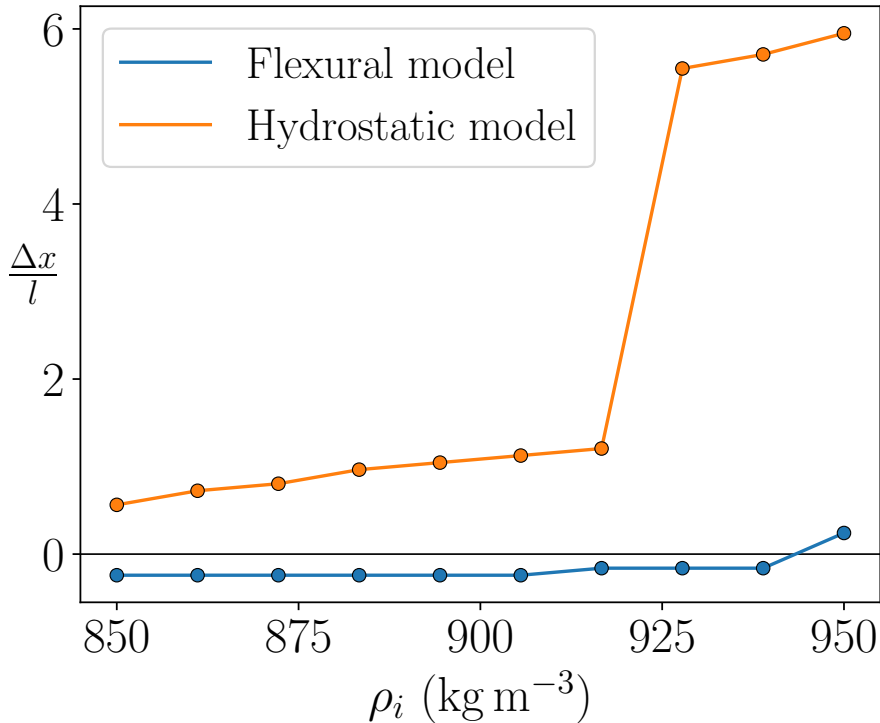


Figure 3.9: Difference between modelled and observed grounding line positions in units of the bending buoyancy length scale l , as a function of ice density ρ_i . Inversions were performed using radio-echo surface data

ice base lies within the BedMachine uncertainty region, supporting its use to measure the bedrock height.

In the ground ice sheet, both inversions predict the existence of an elastically-supported cavity immediately upstream of the grounding line. Analysis of the curvature of surface ice can reveal the subglacial hydrological networks upstream of the grounding line (Remy and Legresy, 2004), and similarly-sized cavities at the grounding zone have been observed in Thwaites Glacier, such as the cavity approximately $10 \times 4 \times 0.35$ km in size that formed between 2011 and 2016 at the grounding line just 10 km from the transect AA' (Milillo et al., 2019). However, the radio-echo data do not support the existence of such a cavity along the transect AA' in this case.

By better-constraining the ice thickness near the grounding line of the Thwaites ice sheet, the flexural model improves the melt rate estimates there. The hydrostatic model predicts a melt rate of $\sim 1000 \text{ m yr}^{-1}$ in the grounding zone, whereas the flexural model predicts melt rates of $\sim 100 \text{ m yr}^{-1}$ in this region for both inversions (see inset in Figure 3.7D). The inverted melt rates are also significantly lower than the hydrostatic model far from the grounding zone. The average melt rate along the Thwaites transect is shown in Table 3.1, along with the average melt rates of the other ice shelves considered in this dissertation.

The radio-echo data reveal that the undersides of the ice shelves are rough, showing thickness variations analogous to small-scale topography on the surface of the Earth. If the ice shelf is assumed to be complete hydrostatic equilibrium far from the grounding zone, this ‘topography’ on the underside of the ice shelves implies the density of ice varies by $\sim 20 \text{ kg m}^{-3}$ along the shelf (Figure 3.5). Moreover, it implies extremely large, varying melt rates of $\pm 2500 \text{ m yr}^{-1}$ far from the grounding zone. In fact, much (or all) of this topography is likely supported by the rigidity of the ice shelf and requires no significant variation in ice density along the shelf or large melt rates.

If these ice thickness variations are steady-state features supported hydrostatically, their persistence over time must be maintained by the large, alternating melting and freezing rates shown in Figure 3.7D. In contrast, if they are supported elastically, they can persist without requiring ongoing melting or refreezing. To evaluate whether the observed ice thickness variations were supported elastically or hydrostatically, the degree of compensation of a periodic load of wavelength λ was calculated using

$$C = \frac{\rho_w - \rho_i}{\rho_w - \rho_i + \frac{B}{g} \left(\frac{2\pi}{\lambda} \right)^4}, \quad (3.1)$$

where C is the degree of compensation and B is the uniform beam bending stiffness (Turcotte and Schubert, 2002, p. 123). The degree of compensation of a topographic load is the ratio of the deflection of the beam to its maximum (hydrostatic) deflection. Figure 3.10 shows compensation curves for thin and thick ice shelves with uniform elastic thicknesses 500 m and 1000 m, respectively.

For these typical ice shelf thicknesses, topographic variations with $\lambda \ll 10 \text{ km}$ are uncompensated ($C = 0$): they are supported entirely by the rigidity of the shelf and cause no shelf deflection. For long-wavelength loads, the ice shelf has no rigidity and is in hydrostatic equilibrium. The critical wavelength below which topography is supported elastically is given by

$$\lambda \ll 2\pi \left(\frac{B}{\rho_i g} \right)^{\frac{1}{4}}, \quad (3.2)$$

(Turcotte and Schubert, 2002, p. 122). From this, we can see that the critical wavelength for elastic support is approximately ten times the bending-buoyancy length-scale calculated in (2.11). As all of the wavelength of the topographic variation along the ice base is significantly less than 10 km, it is likely entirely supported by the rigidity of the ice shelf. Therefore, it is likely that this topographic variation in ice thickness is not maintained in steady-state by large variations in melt rate but instead advects down the ice stream while remaining approximately in equilibrium with the surrounding ocean water. As this elastically-supported roughness on the underside of the ice does not

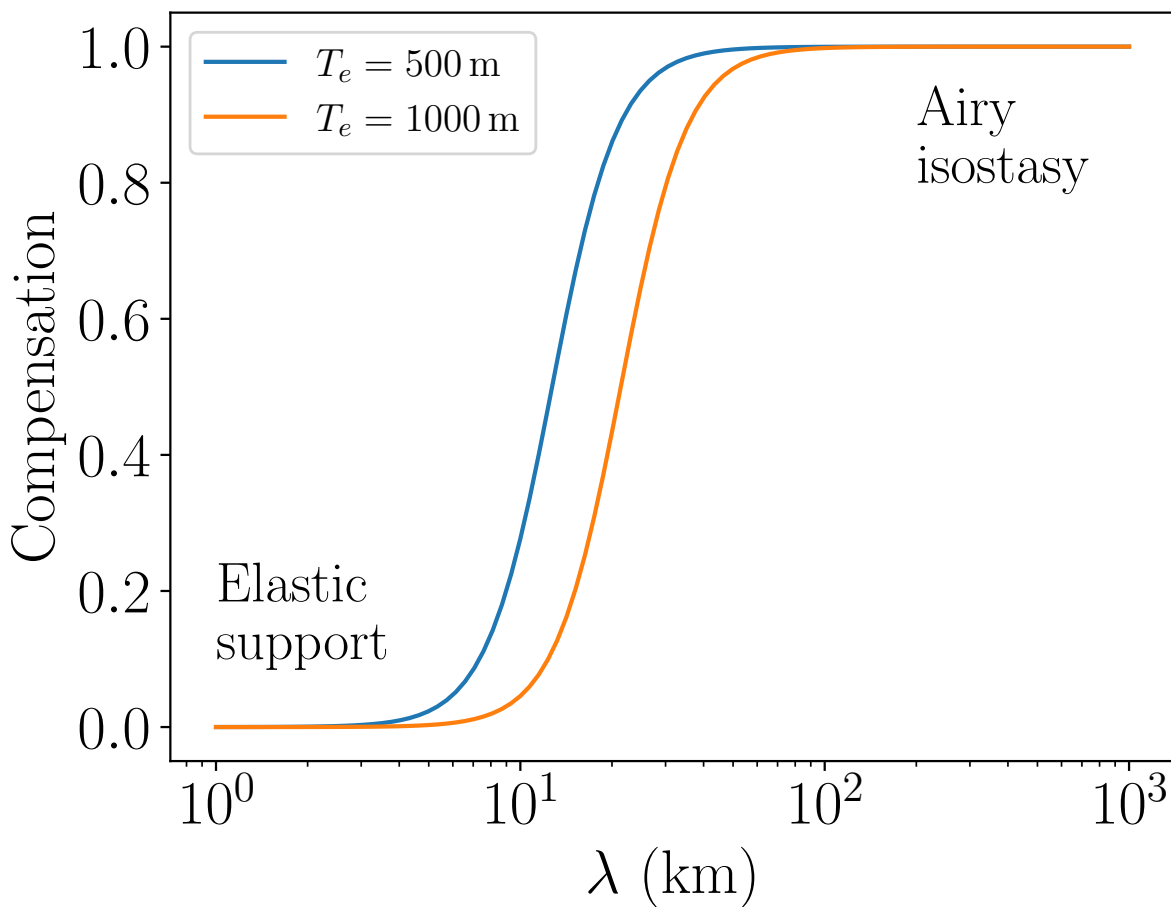


Figure 3.10: Dependence of the degree of compensation C on the wavelength λ of periodic topography on an elastic ice shelf. The shelf has density $\rho_i = 917 \text{ kg m}^{-3}$, Young's modulus $E = 1.6 \text{ GPa}$ and thickness T_e floating on a liquid of density $\rho_w = 1027 \text{ kg m}^{-3}$.

produce a corresponding expression at the ice surface, its shape cannot be inferred from inversions using surface elevation data. Therefore, we should not expect the model to be able to reproduce the rough undersides of ice shelves. This violation of the steady-state assumption highlights the limitations of the steady-state approach of inferring melt rates.

The hydrostatic model shows similarly large variations in melt rate as the radio-echo data far from the grounding zone. These large melt rates are due to the large isostatically-compensated cavities predicted by the hydrostatic model in response to variations in the observed surface elevation at ~ 20 km along the transect. As in the grounding zone, the flexural model supports these surface elevation variations elastically, and products a smooth ice base. The large increase in melt rate predicted by the hydrostatic model at ~ 5 km is due to the . This behaviour is discussed further in Section 3.6, and is also responsible for the sinusoidal variations in inverted melt rate far from the grounding zone.

3.3 Pine Island Glacier

With the model parameters fitted at Thwaites Glacier, the flexural model was applied to other glaciers in the Amundsen Sea embayment (Figure 3.1). Figure 3.11 shows the BedMachine and radio-echo data along the Pine Island transect BB' . The inversion process did not converge to a solution along this transect; specifically, the outer iteration failed to converge to local ϵ_s and ϵ_b minima. This implies that these objective functions are highly non-linear and that the Newton-Raphson method cannot find their roots using the starting $h^{\text{init}}(x)$ and $b_0^{\text{init}}(x)$ profiles described in Section 2.2. One reason for this lack of convergence may be the extended length of the Pine Island transect compared to the other transects considered in this dissertation.

The radio-echo data reveal large variations along the underside of the Pine Island Glacier. Without an estimate of the radio-echo data uncertainty, it is unclear whether these variations reflect genuine changes in ice thickness or are primarily attributable to measurement noise.

3.4 Pope Glacier

Figure 3.12 shows inverted profiles along the Pope Glacier transect CC' . The inversion using the radio-echo surface data (Figure 3.12B) predicted a grounding line position

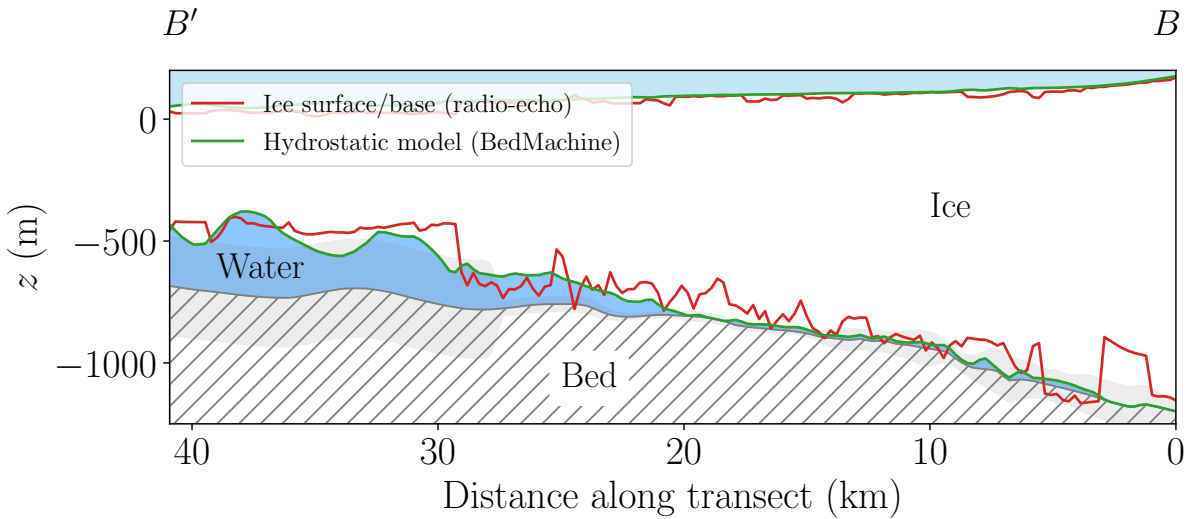


Figure 3.11: Profile along Pine Island transect BB' . Radio-echo ice surface and base data are shown in red, and BedMachine ice surface and hydrostatic base are shown in green.

approximately 7.5 km upstream than the radio-echo ice base suggests. However, the first point of intersection of the radio-echo ice base and BedMachine bedrock height is only slight, and without a knowledge of the radio-echo data uncertainty, it is not clear whether the ice is truly grounded at this position. Moreover, the radio-echo ice base lies approximately 200 m below the BedMachine bedrock height. This disagreement between datasets casts doubt on the validity of one or both of these datasets in this region. It is likely that the BedMachine data are less accurate, as they are interpolated across the entirety of Antarctica as opposed to being measured along a specific transect.

As at Thwaites, the inversion using radio-echo surface data produced a significantly smoother ice base profile than that observed in the radio-echo data. This suggests that the variations in radio-echo ice base are elastically supported, and hence that the spikes in radio-echo melt rates at approximately 7.5 km are not representative of the true steady-state melt rate in Pope Glacier.

The inversion using BedMachine surface data produced a similar profile to that with radio-echo surface data. Both inversions produced melt rate profiles with significantly lower melt rates than those suggested by the radio-echo data.

Pope Glacier

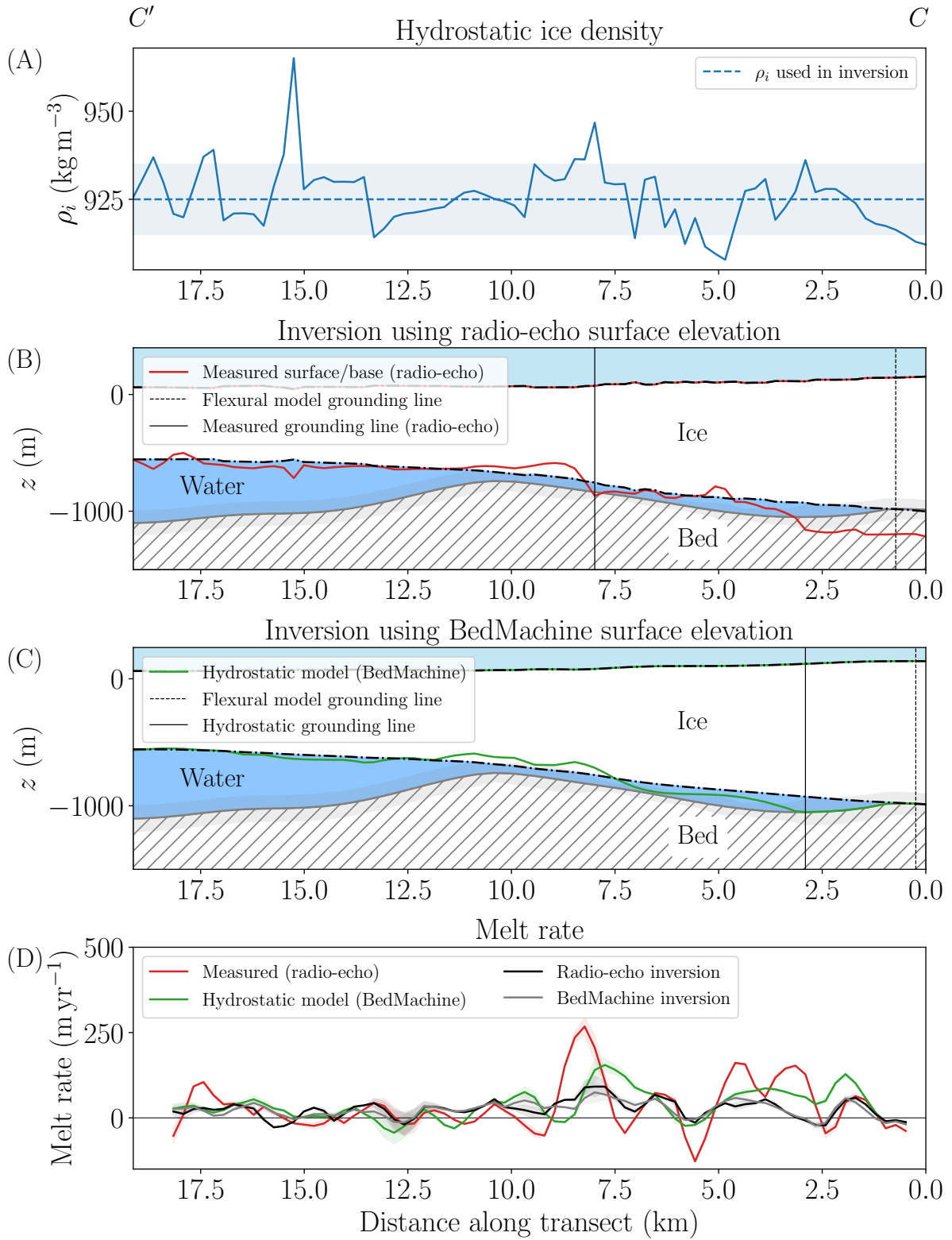


Figure 3.12: (A) Ice density ρ_i inferred from radio-echo ice thickness assuming hydrostatic equilibrium. (B) Inversion for ice shelf profile using radio-echo surface elevation. (C) Inversion for ice shelf profile using BedMachine surface elevation. (D) Melt rate along the transect. Inversions used $\rho_i = 925 \text{ kg m}^{-3}$, $\rho_w = 1027 \text{ kg m}^{-3}$, $E = 1.6 \text{ GPa}$ and $k/\rho_i g = 10^5$. Ice flow is right to left.

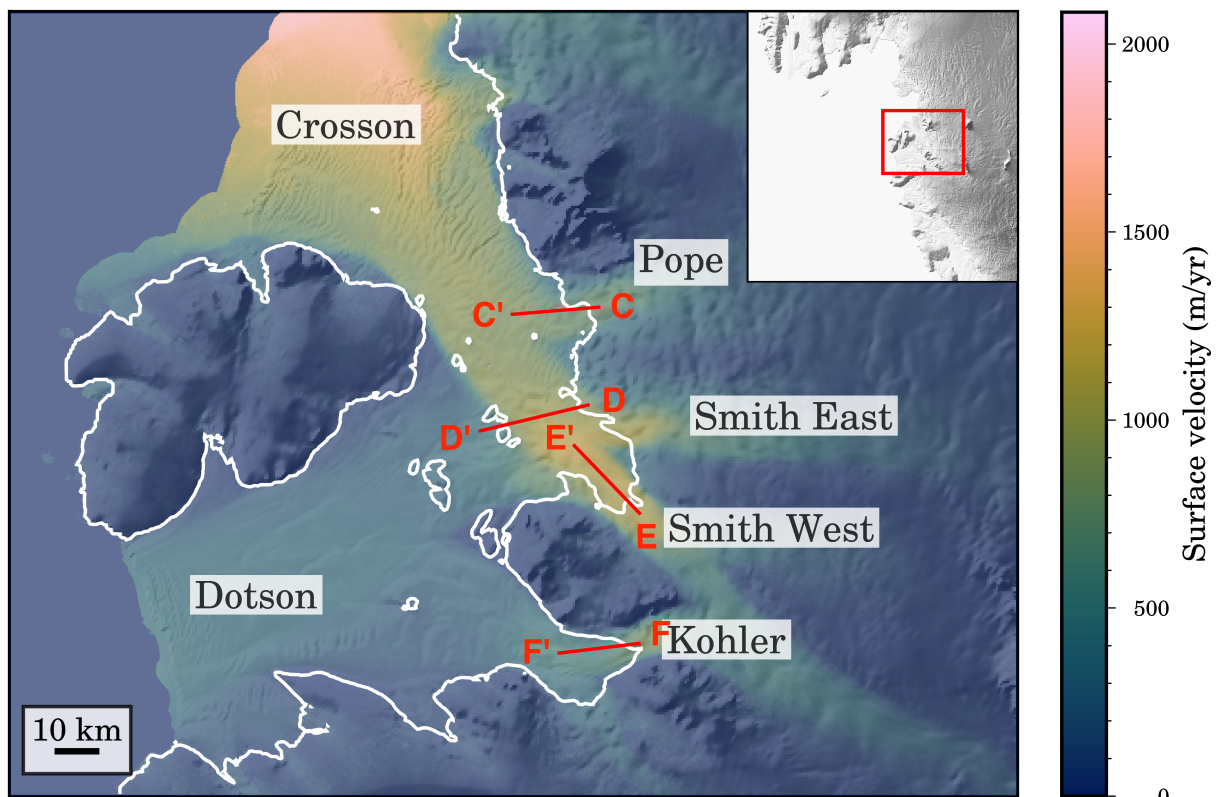


Figure 3.13: BedMachine surface elevation and ITS_LIVE ice surface velocities of the glaciers flowing into the Crosson and Dotson ice sheets. Inset shows location of Crosson and Dotson ice sheets within the Amundsen Sea embayment. The hydrostatic grounding line (using $\rho_i = 917 \text{ kg m}^{-3}$ and $\rho_w = 1027 \text{ kg m}^{-3}$) is shown in white.

3.5 Smith East Glacier

Figure 3.15 shows inversions for a Smith East glacier profile along the transect DD' . At this location, the hydrostatic grounding line suggests that the ice re-grounds at a pinning point in the centre of the ice stream (Figure 3.13). The hydrostatic ice density (Figure 3.15A) increases along the transect to $\sim 975 \text{ kg m}^{-3}$ at the pinning point, and the surface ice velocity decreases by $\sim 400 \text{ m yr}^{-1}$ across the same region (Figure 3.14). The flexural model requires a single uniform ice density, so a more physical ice density of 925 kg m^{-3} typical of the rightmost region of the transect was used for the inversion process.

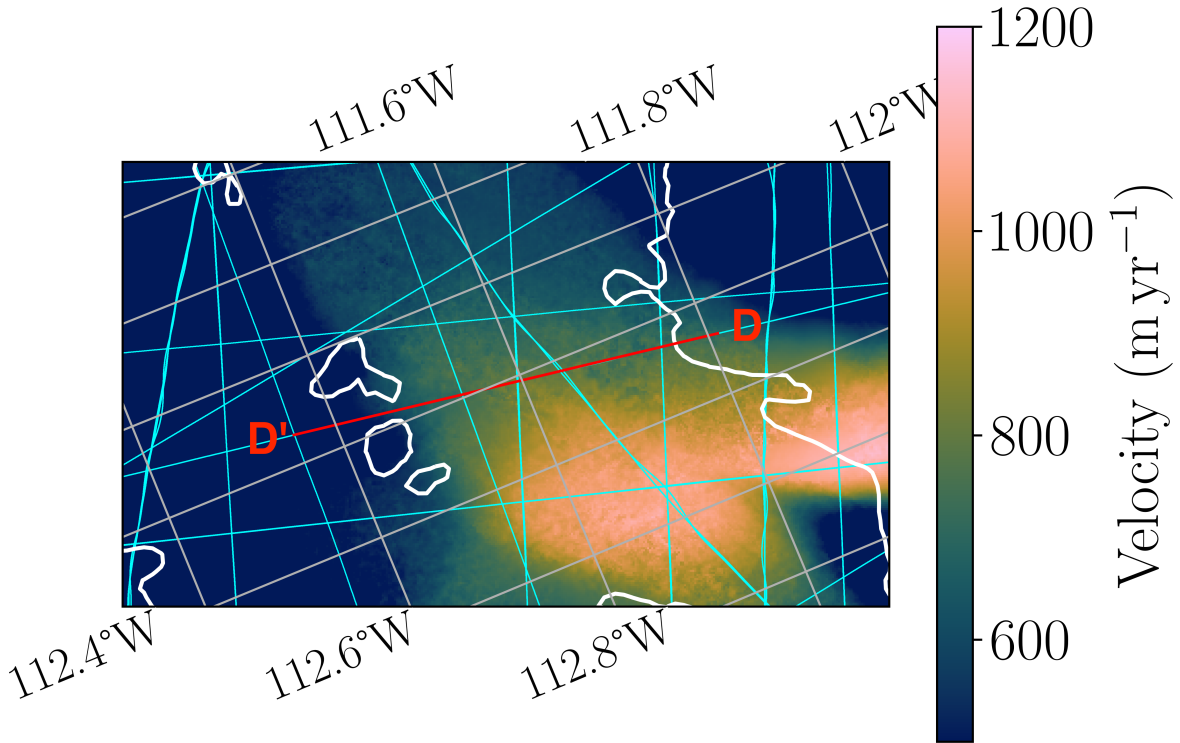


Figure 3.14: Surface ice velocity in the direction of the Smith East transect DD' (i.e. $\mathbf{u}(x, z_m + h/2) \cdot \hat{\mathbf{t}}$). Transect DD' shown in red. Hydrostatically-inferred grounding line shown in white. Radio-echo flight lines shown in cyan.

The inversion using radio-echo surface data (Figure 3.15B) shows a poor fit to the radio-echo-derived ice base, which shows sinusoidal height variations of $\sim 500 \text{ m}$ in the grounding zone. Moreover, the inverted ice shelf profile does not re-ground at the pinning point, owing to its low density. The inversion using the BedMachine surface elevation shows a closer fit to the radio-echo-derived ice base; however, it too remains floating at the pinning point. Neither inversion recovers the large sinusoidal variations in ice thickness observed along the transect.

The inverted melt rates are approximately 50 m yr^{-1} across the transect. The observed

melt rate shows rapid apparent melting and freezing in line with the sinusoidal variations in ice thickness. The radio-echo flight lines in Smith East Glacier deviated significantly from the local direction of ice flow. As the model melt rate is calculated along the transect direction only, it may be unrepresentative of the true melt rate in the direction of ice flow.

The simultaneous increase in hydrostatic ice density and decrease in ice surface velocity towards the pinning point suggests the ice is compacted near the pinning point, owing to a buttressing (backstress) force provided by the pinning point. To test whether the sinusoidal thickness variations are due to ice shelf buckling due to the backstresses provided by this pinning point, characteristic horizontal loads P were estimated for Smith East Glacier and compared with the theoretical critical buckling load for an elastic plate (Turcotte and Schubert, 2002, p. 119),

$$P_c = \frac{\pi^2}{L^2} B, \quad (3.3)$$

where L is the length of the beam. Taking $L = 20$ km, the critical horizontal load for buckling of the Smith East ice shelf is ~ 3 GPa m. To calculate the characteristic horizontal loads in the Smith East Glacier, typical strain rates were estimated using

$$\varepsilon_{xx} = \frac{du}{dx}. \quad (3.4)$$

From Figure 3.14, characteristic velocity changes $\Delta u \sim 200$ m yr $^{-1}$ occur over characteristic length $\Delta l \sim 10$ km. Therefore, $\varepsilon_{xx} \sim 6 \times 10^{-10}$ s $^{-1}$. Taking $E \approx 1$ GPa, The horizontal normal stress is $\sigma_{xx} \sim 0.6$ GPa s $^{-1}$. Finally, the horizontal load through the ice shelf scales like $P \sim \sigma_{xx} h \sim 600$ Pa m. As $P \ll P_c$, the horizontal loads in the Smith East ice stream are unlikely to be causing the observed sinusoidal ice thickness variations.

These thickness variations have a wavelength of approximately 5 km. Therefore, the compensation analysis of Figure 3.10 suggests they ought to be elastically supported. However, applying a hydrostatic model to the radio-echo surface data produces an ice base with the same sinusoidal appearance as the observed ice base (Figure 3.16). The ice base suggested by the hydrostatic model contains the same large variations in ice base elevation as the observed radio-echo data, suggesting that these features are in hydrostatic equilibrium. These features were identified as potential basal crevasses by Surawy-Stepney et al. (2023), and their surface expression is visible in Figure 3.13.

The smooth ice base predicted by the flexural model implies it supports these variations in surface height elastically rather than hydrostatically, as appears to be the case in

Smith East Glacier

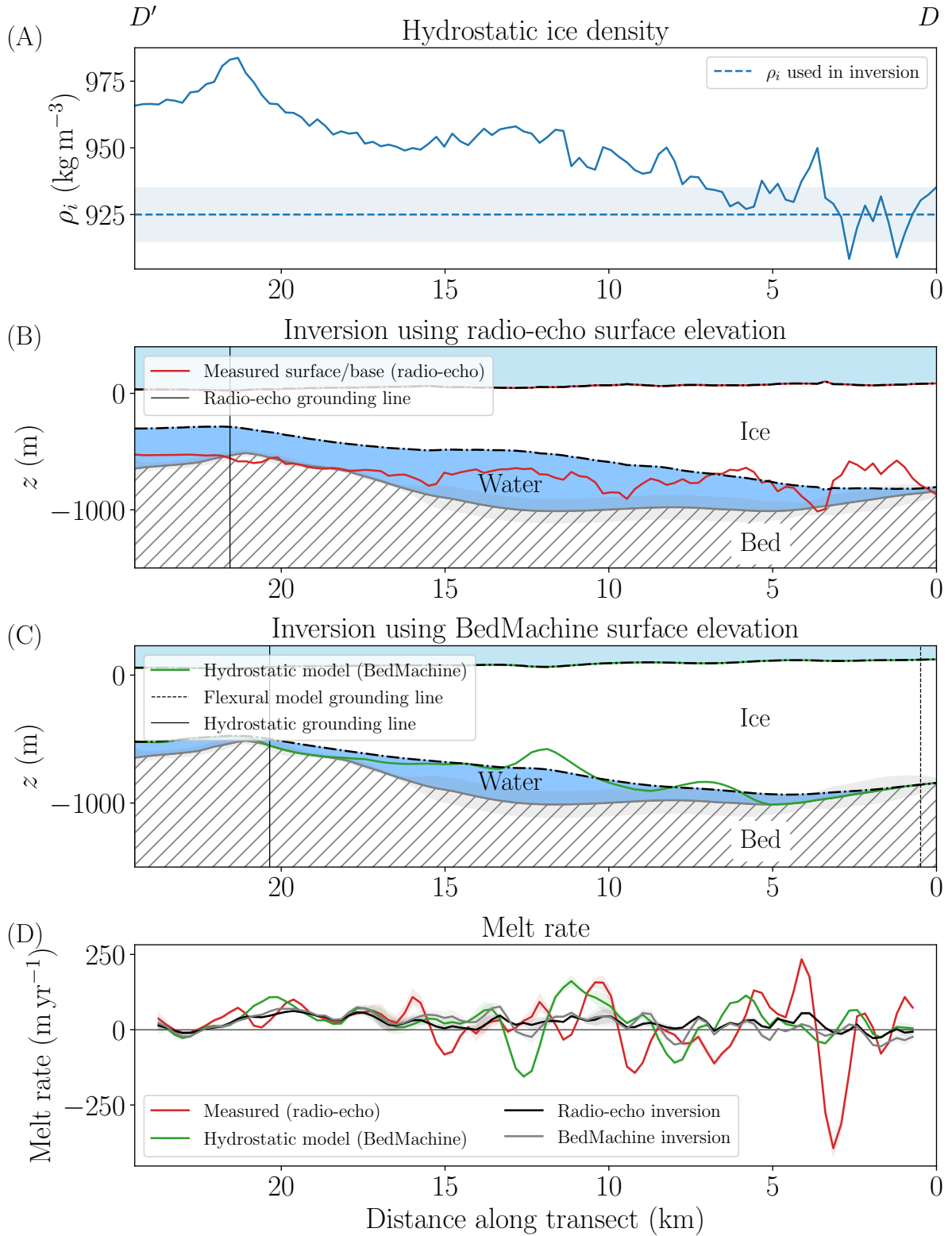


Figure 3.15: (A) Ice density ρ_i inferred from radio-echo ice thickness assuming hydrostatic equilibrium. (B) Inversion for ice shelf profile using radio-echo surface elevation. (C) Inversion for ice shelf profile using BedMachine surface elevation. (D) Melt rate along the transect. Inversions used $\rho_i = 925 \text{ kg m}^{-3}$, $\rho_w = 1027 \text{ kg m}^{-3}$, $E = 1.6 \text{ GPa}$ and $k/\rho_i g = 10^5$. Ice flow is right to left.

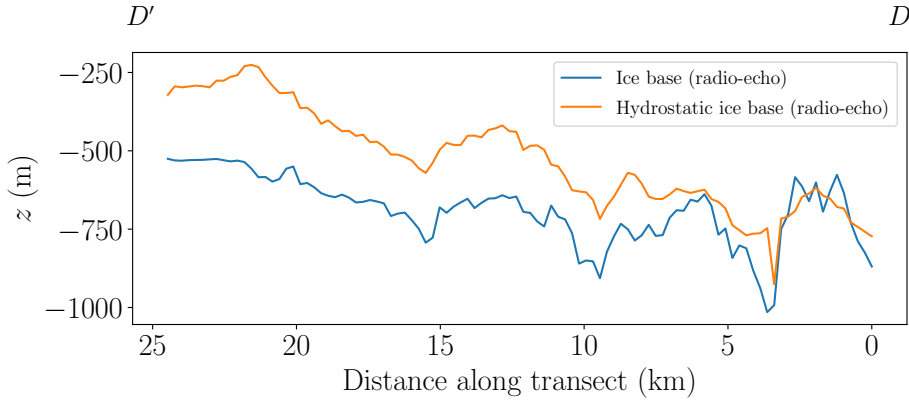


Figure 3.16: Measured ice base (blue) and ice base predicted by a hydrostatic model using $\rho_i = 925 \text{ kg m}^{-3}$ (orange) along the Smith East transect DD' . The large variations in ice base elevation are clearly present in the hydrostatic model, confirming their hydrostatic support.

reality. To test whether this was the case, the residual force was calculated along the inverted shelf profile. Any elastically supported variations in inverted ice shelf thickness would produce a residual force and associated gravity anomaly (Fowler, 2004, ch. 5). From equation (2.13), the residual force R along the shelf is given by

$$R = -\gamma \frac{d^2}{dx^2} \left(h^3 \frac{d^2 z_m}{dx^2} \right) - \rho_i g h + k \left(\frac{h}{2} - z_m - b_0 \right) \mathbb{1}(h/2 - z_m - b_0) + \rho_w g \left(\frac{h}{2} - z_m \right) \mathbb{1}(h/2 - z_m). \quad (3.5)$$

Figure 3.17 shows the residual force along the inverted Smith East flexural model profile. There are positive and negative residual force anomalies that closely resemble the variation in surface elevation used in the inversion process. This confirms the flexural model supports these variations of wavelength $\sim 5 \text{ km}$ in surface elevation elastically, as suggested by Figure 3.10. This elastic support produces the smooth ice base and residual forces observed in the flexural model. In reality, these variations in surface elevation are likely isostatic expressions of variations in ice thickness caused by crevassing and abrasion at the ice base, with the surface elevation maxima and minima aligning with the thick ice ‘roots’ and shallow cavities observed by radio-echo sounding. In this way, the ice shelf shows Airy-type compensation analogous to compensation of topographic loads on the lithosphere; however, the direction of loading in the ice shelf is inverted compared to the lithosphere, with negative loading on the underside of the shelf by crevassing and abrasion causing a compensating change in surface elevation.

Calculating the residual force in the inverted ice shelf provides a method of quantifying the accuracy of the inverted model profile along the transect: if the ice shelf is assumed to be in hydrostatic equilibrium far from the grounding line, its residual force balance ought

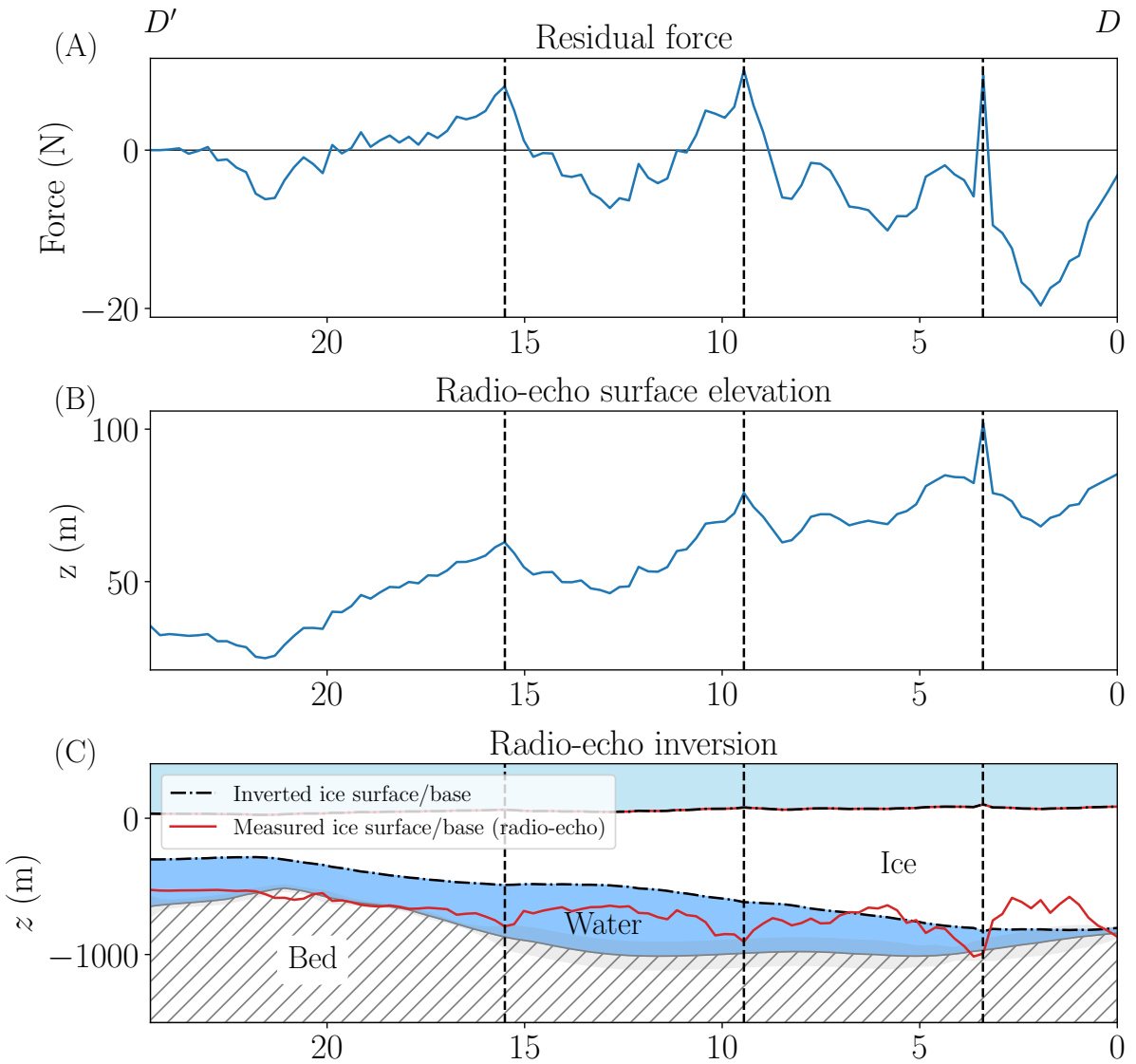


Figure 3.17: (A) Residual force. (B) Radio-echo surface elevation. (C) Inversion for ice shelf profile using radio-echo surface elevation, as in Figure 3.15D. Dashed lines highlight positive residual force anomalies.

be close to zero. Therefore, any large residual force anomalies far from the grounding line indicate an uncompensated (non-isostatic) feature in the inverted ice shelf profile. Future work may incorporate the minimisation of the residual force anomaly far from the grounding zone into the inversion process. This would produce ice shelf profiles that more accurately reproduce the roughness on the base of the ice due to crevassing/abrasion where this deformation of the ice shelf is isostatically supported, as in Smith East glacier. However, this method would not reproduce elastically-supported small-wavelength roughness like that observed in the leftmost end of the Thwaites transect (Figure 3.7B), as they produce no expression on the surface of the ice from which to infer their existence.

As Smith East ice shelf cannot support topographic loads of 5 km elastically, it is likely weaker than predicted by the Young's modulus fitting process at Thwaites. Effective Young's moduli as low as 0.8 GPa have been reported in Antarctic ice shelves (Schmeltz et al., 2002), and Figure 3.18 shows a compensation curve for a weak ice shelf with this Young's modulus. The curve shifts to the left as the Young's modulus of the ice decreases, lowering the wavelength of topography that can be supported elastically. However, this analysis suggests that even an ice shelf of Young's modulus 0.8 GPa and thickness 500 m ought to predominantly support topographic loads of wavelength 5 km elastically, suggesting the true effective Young's modulus for this region is lower than 0.8 GPa. A combination of ice weakening and thinning may further shift the compensation curve to the left; this would produce a range of likely effective Young's moduli and thicknesses in the Smith East region that may be used for future inversions.

As discussed at Thwaites, the crevasses observed at Smith East are not steady-state features, but advect downstream with the ice. The flexural model has no time dependence so incorrectly interprets these large variations in ice thickness as steady-state features that require large variations in steady-state melting along the ice shelf to be maintained.

3.6 Smith West Glacier

Figure 3.19 shows inversions for a Smith West glacier profile along the transect EE' . A characteristic ice density of $\rho_i = 930 \text{ kg m}^{-3}$ was used for the inversion process. An inversion using radio-echo surface data was not performed along this transect as some radar data were unavailable. The BedMachine inversion (Figure 3.19B) predicted a grounding line approximately 5 km upstream compared with the hydrostatic model (3.19B, lower green line). The melt rate showed large sinusoidal variations along the transect of order 200 m in the grounding zone. As the inverted ice thickness is relatively constant along

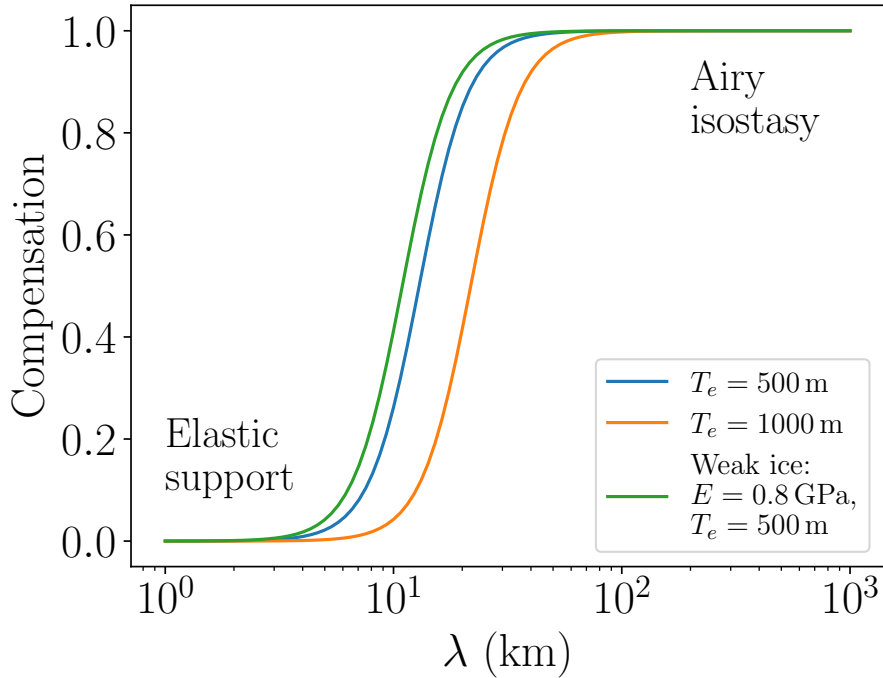


Figure 3.18: Compensation curves as in Figure 3.10, with a curve for weak ice of effective Young's modulus $E = 0.8 \text{ GPa}$.

the transect, this variation in melt rate is due to variations in surface ice velocity. This amplitude of this melting signal is significantly larger than the $40\text{--}70 \text{ m yr}^{-1}$ of melting measured by Khazendar et al. (2016) across Smith Glacier. They measured basal melting by comparing radio-echo-derived ice thicknesses from 2002 and 2009 in Smith Glacier. The large discrepancy between these values suggests at least one model assumption is violated. It is likely that it is the steady-state ($\partial h / \partial t = 0$) assumption that is being violated, as Khazendar et al. (2016) demonstrate that melting is intensely far from steady-state in the grounding zones of ice shelves in the Amundsen Sea embayment, particularly in Smith Glacier. Furthermore, the basal melting measurement method taken by Khazendar et al. (2016) produces an spatially-averaged melt rate. Performing a similar spatial average across the Smith West transect produces an average melt rate of 21 m yr^{-1} , more closely in line with (and lower than) the melt rates reported in Khazendar et al. (2016).

Figure 3.20 shows the surface ice velocity in the direction of the Smith West transect. The velocity varies across the ice stream with high spatial frequency, and there is a localised high velocity region in the centre of the ice stream. The initial velocity increase appears to occur in a grounded region, at approximately 2.5 km along the transect. Although sparse, the radio-echo data in this region show no significant change in ice thickness at this point; therefore, this speed-up is likely attributable to a rapid increase in basal sliding speed. Possible reasons for a rapid increase in velocity in the centre of the ice stream include a decrease in the bedrock strength or roughness, or the presence of water and an

increase in water pressure. When the ice is floating, changing buttressing effects from the sidewalls of the ice stream may be responsible for the velocity variation.

Downstream from the grounding line, the observed velocity variations appear coincident with the changes in radio-echo-derived ice thickness. Specifically, ice thinning is coincident with an increase in ice surface velocity. These variations in ice thickness show a similar morphology to the crevasses observed at Smith East, and are likely hydrostatically supported. The observed inverse proportionality of ice thickness and velocity changes likely arises from the steady-state conservation of mass,

$$\frac{\partial}{\partial x}(uh) = a. \quad (3.6)$$

As gradients in the product uh balance melting, one would expect the observed inverse proportionality of u and h if the melt rate across the shelf were approximately constant. This analysis suggests that the observed large variations in melt rate are likely spurious, and that a more accurate melt rate for Smith West is the average value of 21 m yr^{-1} . The model produces such large melt rates because it cannot reproduce the variations in ice thickness along the shelf observed by radio-echo sounding. The BedMachine surface data do not appear to contain the surface expression of these hydrostatically-supported crevasses, limiting the ice thickness information that may be inverted for. Even if radio-echo data were available along this transect, the flexural model would likely still support the $\sim 5 \text{ km}$ variations in surface elevation elastically, as seen at Smith East, and thus yield a similarly smooth profile of approximately constant thickness. This highlights the importance of using accurate surface observations during the inversion process and carefully tuning the model's elastic parameters to determine how periodic loading (i.e. crevassing) of various wavelengths is compensated by the ice sheet. Future work may use a combination of methods to determine the appropriate effective Young's modulus E for a specific ice shelf. One approach may be to observe the wavelength of the surface expression of isostatically-supported crevasses and to use a compensation-type analysis similar to Figure 3.18 to determine an appropriate E value specific to that location.

3.7 Kohler Glacier

Figure 3.21 shows inversions for a Kohler glacier profile along the transect FF' . A uniform ice density of 940 kg m^{-3} is consistent with the observed hydrostatic ice density (Figure 3.21A). The inversion using the radio-echo surface data predicts a grounding line position approximately 4 km upstream from that suggested by the radio-echo ice base

Smith West Glacier

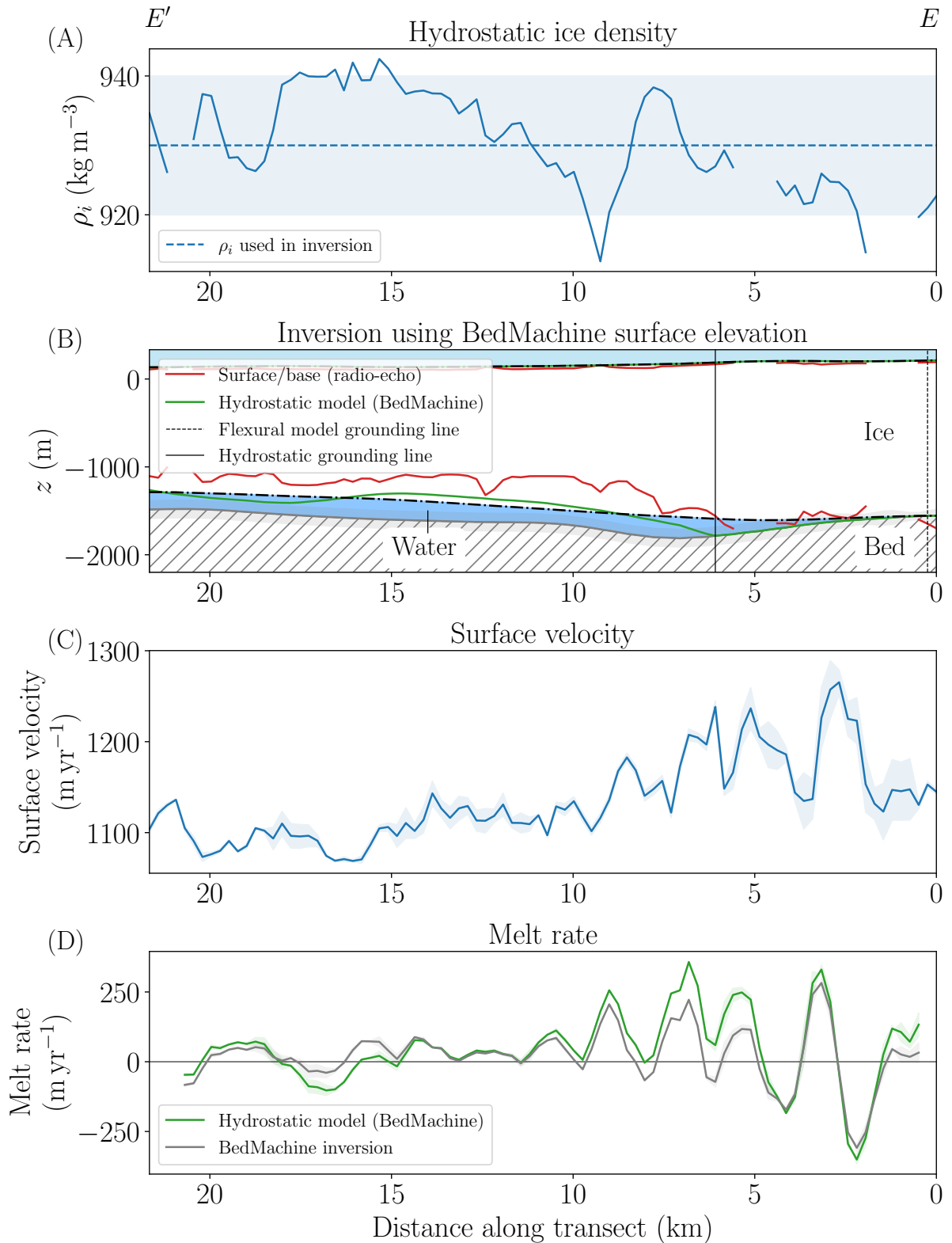


Figure 3.19: (A) Ice density ρ_i inferred from radio-echo ice thickness assuming hydrostatic equilibrium. (B) Inversion for ice shelf profile using BedMachine surface elevation. (C) Surface velocity along the transect. (D) Melt rate along the transect. Inversions used $\rho_i = 930 \text{ kg m}^{-3}$, $\rho_w = 1027 \text{ kg m}^{-3}$, $E = 1.6 \text{ GPa}$ and $k/\rho_i g = 10^5$. Ice flow is right to left.

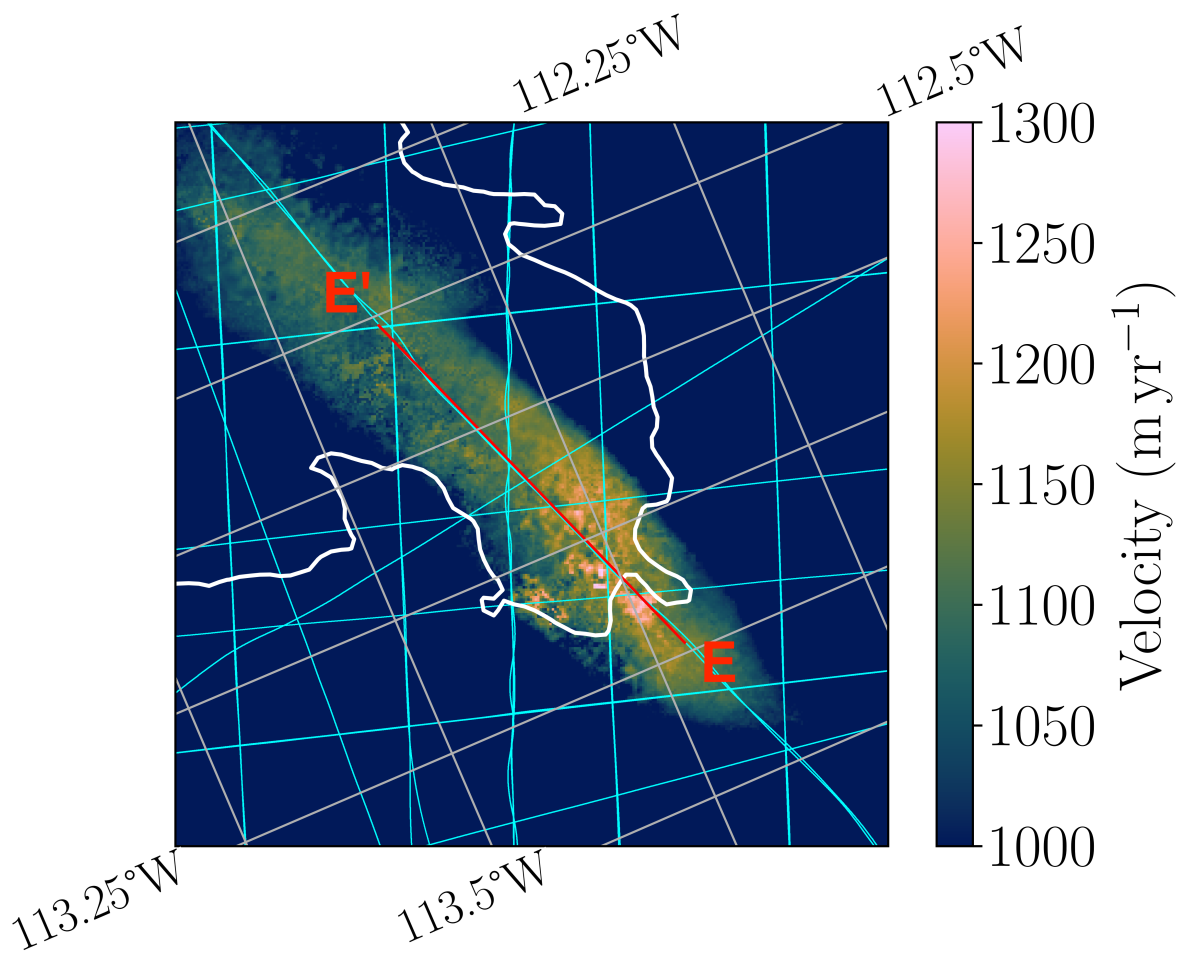


Figure 3.20: Ice surface velocity in the direction of the Smith West transect EE' (i.e. $\mathbf{u}(x, z_m + h/2) \cdot \hat{\mathbf{t}}$). Transect EE' shown in red. Hydrostatic grounding line shown in white. Radio-echo flight lines shown in cyan.

data. The inversion using the BedMachine surface data shows a similar re-evaluation of the grounding line position.

In the grounding zone, both inversions predict melt rates of approximately half that suggested by the hydrostatic model, at approximately 100 m yr^{-1} . This value is still significantly larger than the $14\text{--}29 \text{ m yr}^{-1}$ calculated by Khazendar et al. (2016) in the grounding zone of Kohler Glacier. As discussed at Smith Glacier, it is likely that the discrepancy between these values arises from the model assumption of steady-state and the lack of spatial averaging of the melt rate. The spatially-averaged melt rate along the transect is 42 m yr^{-1} for the radio-echo inversion and 37 m yr^{-1} for the BedMachine inversion. Both of these melt rates are larger than those reported by Khazendar et al. (2016).

Both inversions predicted a clear reduction in melt rate predicted in the grounding zone of Kohler Glacier. However, the radio-echo-derived ice base extends below the BedMachine bed topography height beyond its error range. Without knowing the error of the radio-echo data, it is not possible to determine whether this discrepancy is within a suitable error range. However, as the BedMachine dataset is interpolated across Antarctica using a mass conservation approach (Morlighem, 2022), it is likely that these data are less accurate than the radio-echo data. Future work might create more accurate bed topography maps across Antarctica. For example, a deep-learning method developed by Van Pelt et al. (2013) allows higher-order ice flow physics to be incorporated into the inversion process for grounded ice thickness. This method has been used to create state-of-the-art bed topography maps in Svalbard and Scandinavia (Van Pelt and Frank, 2025; Frank and Van Pelt, 2024) and could be applied to Antarctica to improve estimates of bed topography height.

3.8 Average melt rates

Table 3.1 shows the spatially-average melt rates calculated along the transects of the glaciers considered in this dissertation. The radio-echo and BedMachine flexural model inversions show a reduction in average melt rate at each glacier compared to the hydrostatic model. The flexural models showed the largest improvement (i.e. similarity to the observed average melt rate) at Thwaites Glacier. This is likely due to the model being tuned at this location, along with the fact that Thwaites showed a clear elastic flexural signal and no significant compaction or other longitudinal buttressing forces. The flexural models performed poorly at Smith West glacier, likely owing to the significant

Kohler Glacier

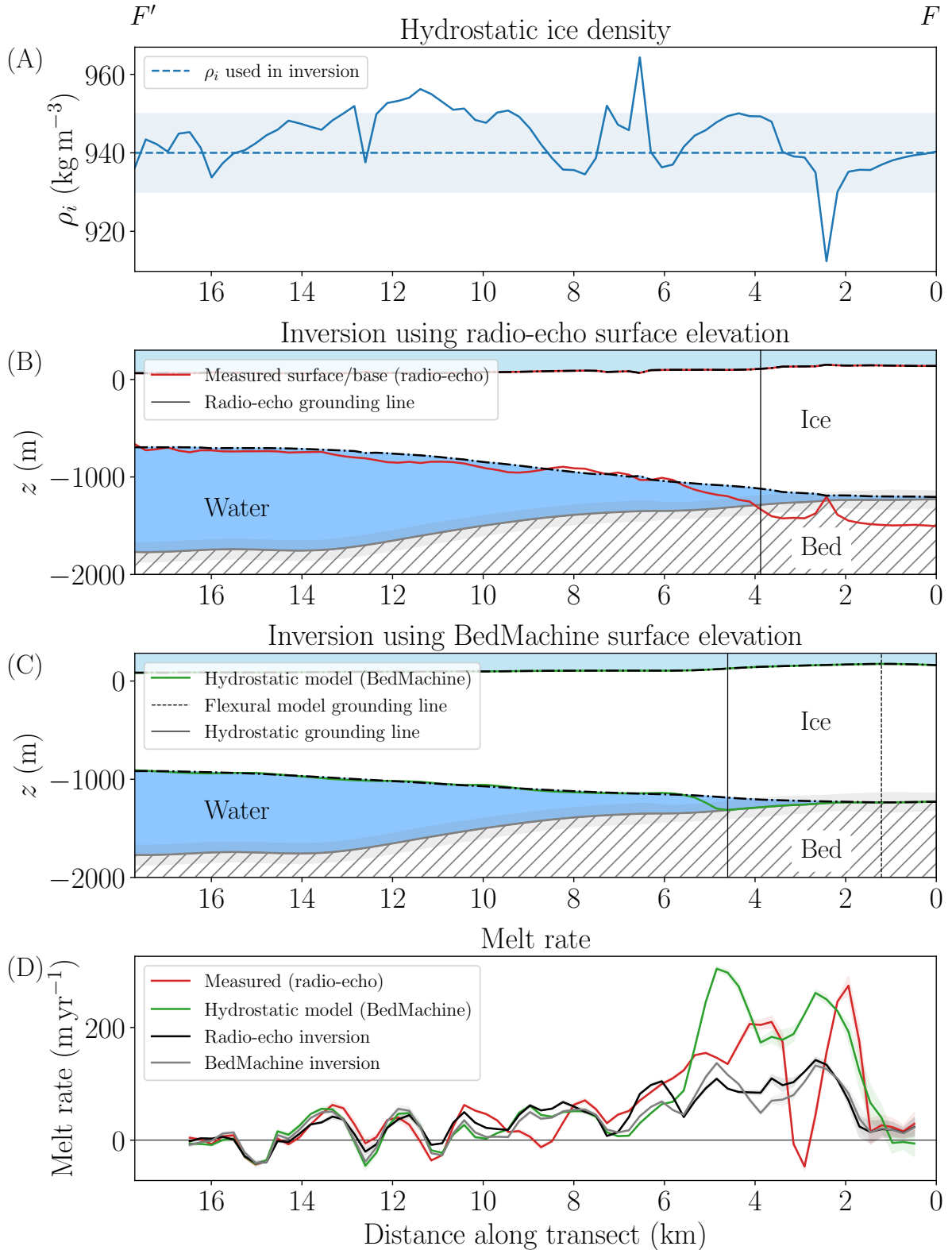


Figure 3.21: (A) Ice density ρ_i inferred from radio-echo ice thickness assuming hydrostatic equilibrium. (B) Inversion for ice shelf profile using radio-echo surface elevation. (C) Inversion for ice shelf profile using BedMachine surface elevation. (D) Melt rate along the transect. Inversions used $\rho_i = 940 \text{ kg m}^{-3}$, $\rho_w = 1027 \text{ kg m}^{-3}$, $E = 1.6 \text{ GPa}$ and $k/\rho_i g = 10^5$. Ice flow is right to left.

Glacier	Avg. melt rate (radio-echo; m yr ⁻¹)	Avg. melt rate (BedMachine; m yr ⁻¹)	Avg. melt rate (hydrostatic model; m yr ⁻¹)	Avg. melt rate (observed; m yr ⁻¹)	Literature value
Thwaites	-45 (-46, -44)	-64 (-65, -63)	107 (105, 110)	-68	5 to 26*
Pope	25 (23, 26)	24 (23, 26)	37 (36, 38)	34 (33, 35)	29 to 36†
Smith East	22 (21, 22)	20	27 (26, 29)	17 (17, 18)	40 to 70†
Smith West	32 (30, 33)	21 (19, 23)	53 (51, 55)	63 (62, 63)	40 to 70†
Kohler	42 (40, 44)	37 (35, 39)	67 (64, 71)	56 (53, 59)	14 to 29†

Table 3.1: Spatially-averaged melt rates along the transects of the glaciers examined in this dissertation. Melt rate estimates are shown using i) radio-echo inversion, ii) BedMachine inversion, iii) hydrostatic model, iv) observed ice thickness profile. Melt rate ranges are shown in parentheses. *(Schmidt et al., 2023) †(Khazendar et al., 2016).

longitudinal forces present in this region not accounted for by the flexural models. The models performed poorly compared to melt rates from the literature. However, these literature values were not derived from the same transects considered in this dissertation, and are often spatially averaged across entire ice shelves. In fact, melting is highly heterogeneous across the grounding zones of ice shelves (Schmidt et al., 2023), and the flexural model proposed in this dissertation provides a new method of determining this pattern of melting across Antarctica.

Chapter 4

Conclusions and future work

In this dissertation, a novel approach for quantifying melt rates in the grounding zones of Antarctic ice shelves was proposed and applied to a selection of ice shelves. The model uses a force balance that includes the elastic flexure of the ice shelf to invert for its static thickness.

The flexural model closely recovered the analytical deflection profile of a uniform ice shelf resting on a sloping bed, confirming its ability to account for elastic flexure in ice shelves. Moreover, it produced a significantly improved ice thickness and melt profile over the hydrostatic model along a transect through Thwaites Glacier. A sensitivity analysis performed in Thwaites Glacier showed the model robustly predicted the position of the grounding line there compared to the hydrostatic model; however, future work may extend this sensitivity analysis to other bed topographies of varying complexities to determine the robustness of the flexural grounding line position in different settings.

This approach did not model the complex subglacial hydrological networks beneath Antarctic ice shelves. Future work may incorporate the effect of these networks on the melting dynamics of ice shelves, perhaps using measurements of the curvature of the ice surface to infer the shape of the hydrological system beneath Antarctic ice shelves.

The flexural model could not invert for elastically-supported roughness on the underside of ice shelves. This likely caused little variation in the inferred melt rate, as these crevasses are likely not maintained in steady-state by rapid freezing and melting along the ice shelf profile, but instead advect along the ice shelf while experiencing relatively constant rates of melting. This advection may be observed by taking multiple radio-echo soundings along the same transect at different times.

The model failed to converge in one of the six ice shelves studied (Pine Island). To improve model stability, future work may incorporate additional regularisation methods (smoothing and damping) and more stable root-finding methods (such as Brent’s method) into the inversion process.

The inversion at Smith East Glacier revealed the likely influence of longitudinal back-stresses modifying the shape and density structure of the ice shelf. The flexural model performs a purely vertical force balance, so does not account for these longitudinal forces. Future work may involve incorporating such forces to improve the ice shelf profile. The large variation in density along the Smith East ice shelf, likely owing to compaction as the ice re-grounded at a pinning point, was also not accounted for in the flexural model, which treats ice as incompressible. Future work may consider inverting for the density structure of ice, though it is not clear how this may be easily performed. A more practical solution would be to only invert along transects which are unlikely to have experienced significant compaction. Furthermore, the flexural model did not predict the isostatic support of crevasses of wavelength $\sim 5\text{ km}$ at Smith East and Smith West, suggesting the true effective Young’s modulus in this region was lower than that predicted by the E fitting process performed at Thwaites. Future work may use the wavelength of observed isostatically-supported crevasses to constrain the effective Young’s modulus of ice at different ice shelves.

The flexural model proposed in this dissertation calculated melt rates along two-dimensional transects. Future work may extend this model to three dimensions and use horizontal divergence to calculate further improved melt rates. Future work may also investigate the appropriate spatial smoothing required to produce accurate melt rates in those regions for which the flexural model does not predict the isostatic support of crevasses.

Finally, the inversions using the radio-echo and BedMachine surface elevation data produced broadly similar ice thickness and melt profiles, with the exception of Smith East Glacier. This highlights the importance of using high-quality surface elevation data for the inversion process, for example to identify isostatically-supported crevasses. Future work may involve creating a more accurate bed topography map of Antarctica, possibly incorporating novel deep-learning approaches.

References

- Adusumilli, S., H. A. Fricker, B. Medley, L. Padman, and M. R. Siegfried (2020, September). Interannual variations in meltwater input to the Southern Ocean from Antarctic ice shelves. *Nature Geoscience* 13(9), 616–620.
- Budd, W. F. and T. H. Jacka (1989). A review of ice rheology for ice sheet modelling. *Cold Regions Science and Technology* 16(2), 107–144.
- Corr, H. F. J., A. Jenkins, K. W. Nicholls, and C. S. M. Doake (2002, April). Precise measurement of changes in ice-shelf thickness by phase-sensitive radar to determine basal melt rates. *Geophysical Research Letters* 29(8).
- Davison, B. J., A. E. Hogg, N. Gourmelen, L. Jakob, J. Wuite, T. Nagler, C. A. Greene, J. Andreasen, and M. E. Engdahl (2023, October). Annual mass budget of Antarctic ice shelves from 1997 to 2021. *Science Advances* 9(41), eadi0186.
- Depoorter, M. A., J. L. Bamber, J. A. Griggs, J. T. M. Lenaerts, S. R. M. Ligtenberg, M. R. Van Den Broeke, and G. Moholdt (2013, October). Calving fluxes and basal melt rates of Antarctic ice shelves. *Nature* 502(7469), 89–92.
- Dryak, M. C. and E. M. Enderlin (2020, June). Analysis of Antarctic Peninsula glacier frontal ablation rates with respect to iceberg melt-inferred variability in ocean conditions. *Journal of Glaciology* 66(257), 457–470.
- Fowler, C. M. R. (2004). *The Solid Earth: An Introduction to Global Geophysics* (2 ed.). Cambridge University Press.
- Frank, T. and W. J. J. Van Pelt (2024). Ice volume and thickness of all Scandinavian glaciers and ice caps. *Journal of Glaciology* 70, e11.
- Friedl, P., F. Weiser, A. Flührer, and M. H. Braun (2020, February). Remote sensing of glacier and ice sheet grounding lines: A review. *Earth-Science Reviews* 201, 102948.

- Gammon, P. H., H. Kieft, M. J. Clouter, and W. W. Denner (1983). Elastic Constants of Artificial and Natural Ice Samples by Brillouin Spectroscopy. *Journal of Glaciology* 29(103), 433–460.
- Gardner, A., M. Fahnestock, and T. Scambos (2022). MEaSUREs ITS_live Regional Glacier and Ice Sheet Surface Velocities, Version 1.
- Gardner, A. S., G. Moholdt, T. Scambos, M. Fahnestock, S. Ligtenberg, M. Van Den Broeke, and J. Nilsson (2018, February). Increased West Antarctic and unchanged East Antarctic ice discharge over the last 7 years. *The Cryosphere* 12(2), 521–547.
- Hetényi, M. (1946). *Beams on elastic foundations: theory with applications in the fields of civil and mechanical engineering*. Ann Arbor, MI: University of Michigan Press.
- Holdsworth, G. (1969). Flexure of a Floating Ice Tongue. *Journal of Glaciology* 8(54), 385–397.
- Howat, I. M., C. Porter, B. E. Smith, M.-J. Noh, and P. Morin (2019). The Reference Elevation Model of Antarctica. *The Cryosphere* 13(2), 665–674.
- Jenkins, A. and C. S. M. Doake (1991, January). Ice-ocean interaction on Ronne Ice Shelf, Antarctica. *Journal of Geophysical Research: Oceans* 96(C1), 791–813.
- Khazendar, A., E. Rignot, D. M. Schroeder, H. Seroussi, M. P. Schodlok, B. Scheuchl, J. Mouginot, T. C. Sutterley, and I. Velicogna (2016, October). Rapid submarine ice melting in the grounding zones of ice shelves in West Antarctica. *Nature Communications* 7(1), 13243.
- LeB. Hooke, R. (1981, November). Flow law for polycrystalline ice in glaciers: Comparison of theoretical predictions, laboratory data, and field measurements. *Reviews of Geophysics* 19(4), 664–672.
- Lilien, D. A., I. Joughin, B. Smith, and N. Gourmelen (2019). Melt at grounding line controls observed and future retreat of Smith, Pope, and Kohler glaciers. *The Cryosphere* 13(11), 2817–2834.
- Mallett, H. K. W., L. Boehme, M. Fedak, K. J. Heywood, D. P. Stevens, and F. Roquet (2018, May). Variation in the Distribution and Properties of Circumpolar Deep Water in the Eastern Amundsen Sea, on Seasonal Timescales, Using Seal-Borne Tags. *Geophysical Research Letters* 45(10), 4982–4990.
- Martín-Español, A., A. Zammit-Mangion, P. J. Clarke, T. Flament, V. Helm, M. A. King, S. B. Luthcke, E. Petrie, F. Rémy, N. Schön, B. Wouters, and J. L. Bamber (2016, February). Spatial and temporal Antarctic Ice Sheet mass trends, glacio-isostatic

- adjustment, and surface processes from a joint inversion of satellite altimeter, gravity, and GPS data. *Journal of Geophysical Research: Earth Surface* 121(2), 182–200.
- Milillo, P., E. Rignot, P. Rizzoli, B. Scheuchl, J. Mouginot, J. Bueso-Bello, and P. Prats-Iraola (2019, January). Heterogeneous retreat and ice melt of Thwaites Glacier, West Antarctica. *Science Advances* 5(1), eaau3433.
- Morlighem, M. (2022). MEaSUREs BedMachine Antarctica, Version 3.
- Morlighem, M., E. Rignot, T. Binder, D. Blankenship, R. Drews, G. Eagles, O. Eisen, F. Ferraccioli, R. Forsberg, P. Fretwell, V. Goel, J. S. Greenbaum, H. Gudmundsson, J. Guo, V. Helm, C. Hofstede, I. Howat, A. Humbert, W. Jokat, N. B. Karlsson, W. S. Lee, K. Matsuoka, R. Millan, J. Mouginot, J. Paden, F. Pattyn, J. Roberts, S. Rosier, A. Ruppel, H. Seroussi, E. C. Smith, D. Steinhage, B. Sun, M. R. V. D. Broeke, T. D. V. Ommen, M. V. Wessem, and D. A. Young (2020, February). Deep glacial troughs and stabilizing ridges unveiled beneath the margins of the Antarctic ice sheet. *Nature Geoscience* 13(2), 132–137.
- Mouginot, J., E. Rignot, and B. Scheuchl (2014, March). Sustained increase in ice discharge from the Amundsen Sea Embayment, West Antarctica, from 1973 to 2013. *Geophysical Research Letters* 41(5), 1576–1584.
- Mouginot, J., B. Scheuchl, and E. Rignot (2017). MEaSUREs Antarctic Boundaries for IPY 2007-2009 from Satellite Radar, Version 2.
- Neckel, N., R. Drews, W. Rack, and D. Steinhage (2012). Basal melting at the Ekström Ice Shelf, Antarctica, estimated from mass flux divergence. *Annals of Glaciology* 53(60), 294–302.
- Oppenheimer, M., B. Glavovic, J. Hinkel, R. van de Wal, A. Magnan, A. Abd-Elgawad, R. Cai, M. Cifuentes-Jara, R. DeConto, T. Ghosh, J. Hay, F. Isla, B. Marzeion, B. Meyssignac, and Z. Sebesvari (2019). Sea Level Rise and Implications for Low-Lying Islands, Coasts and Communities. In H.-O. Pörtner, D. Roberts, V. Masson-Delmotte, P. Zhai, M. Tignor, E. Poloczanska, K. Mintenbeck, A. Alegría, M. Nicolai, A. Okem, J. Petzold, B. Rama, and N. Weyer (Eds.), *IPCC Special Report on the Ocean and Cryosphere in a Changing Climate*, pp. 321–445. Cambridge, UK and New York, NY, USA: Cambridge University Press.
- Paden, J., J. Li, C. Leuschen, F. Rodriguez-Morales, and R. Hale (2010). IceBridge MCoRDS L2 Ice Thickness, Version 1.
- Pritchard, H. D., S. R. M. Ligtenberg, H. A. Fricker, D. G. Vaughan, M. R. Van Den Broeke, and L. Padman (2012, April). Antarctic ice-sheet loss driven by basal melting of ice shelves. *Nature* 484(7395), 502–505.

- Remy, F. and B. Legresy (2004). Subglacial hydrological networks in Antarctica and their impact on ice flow. *Annals of Glaciology* 39, 67–72.
- Rignot, E., S. Jacobs, J. Mouginot, and B. Scheuchl (2013, July). Ice-Shelf Melting Around Antarctica. *Science* 341(6143), 266–270.
- Rignot, E., J. Mouginot, M. Morlighem, H. Seroussi, and B. Scheuchl (2014, May). Widespread, rapid grounding line retreat of Pine Island, Thwaites, Smith, and Kohler glaciers, West Antarctica, from 1992 to 2011. *Geophysical Research Letters* 41(10), 3502–3509.
- Robel, A. A., H. Seroussi, and G. H. Roe (2019, July). Marine ice sheet instability amplifies and skews uncertainty in projections of future sea-level rise. *Proceedings of the National Academy of Sciences* 116(30), 14887–14892.
- Rosier, S. H. R., O. J. Marsh, W. Rack, G. H. Gudmundsson, C. T. Wild, and M. Ryan (2017, October). On the interpretation of ice-shelf flexure measurements. *Journal of Glaciology* 63(241), 783–791.
- Sayag, R. and M. G. Worster (2011, September). Elastic response of a grounded ice sheet coupled to a floating ice shelf. *Physical Review E* 84(3), 036111.
- Schmeltz, M., E. Rignot, and D. MacAyeal (2002). Tidal flexure along ice-sheet margins: comparison of InSAR with an elastic-plate model. *Annals of Glaciology* 34, 202–208.
- Schmidt, B. E., P. Washam, P. E. D. Davis, K. W. Nicholls, D. M. Holland, J. D. Lawrence, K. L. Riverman, J. A. Smith, A. Spears, D. J. G. Dicheck, A. D. Mullen, E. Clyne, B. Yeager, P. Anker, M. R. Meister, B. C. Hurwitz, E. S. Quartini, F. E. Bryson, A. Basinski-Ferris, C. Thomas, J. Wake, D. G. Vaughan, S. Anandakrishnan, E. Rignot, J. Paden, and K. Makinson (2023, February). Heterogeneous melting near the Thwaites Glacier grounding line. *Nature* 614(7948), 471–478.
- Schmidt, K., J. Reimann, N. Tous Ramon, and M. Schwerdt (2018). Geometric Accuracy of Sentinel-1A and 1B Derived from SAR Raw Data with GPS Surveyed Corner Reflector Positions. *Remote Sensing* 10(4).
- Schoof, C. (2007, February). Marine ice-sheet dynamics. Part 1. The case of rapid sliding. *Journal of Fluid Mechanics* 573, 27–55.
- Schlüson, E. M. (1999, February). The structure and mechanical behavior of ice. *JOM* 51(2), 21–27.
- Surawy-Stepney, T., A. E. Hogg, S. L. Cornford, and D. C. Hogg (2023, October). Mapping Antarctic crevasses and their evolution with deep learning applied to satellite radar imagery. *The Cryosphere* 17(10), 4421–4445.

- Thompson, A. F., A. L. Stewart, P. Spence, and K. J. Heywood (2018, December). The Antarctic Slope Current in a Changing Climate. *Reviews of Geophysics* 56(4), 741–770.
- Turcotte, D. and G. Schubert (2002). *Geodynamics* (2 ed.). Cambridge University Press.
- Van De Wal, R. S. W., X. Zhang, S. Minobe, S. Jevrejeva, R. E. M. Riva, C. Little, K. Richter, and M. D. Palmer (2019, November). Uncertainties in Long-Term Twenty-First Century Process-Based Coastal Sea-Level Projections. *Surveys in Geophysics* 40(6), 1655–1671.
- Van Pelt, W. and T. Frank (2025, January). New glacier thickness and bed topography maps for Svalbard. *The Cryosphere* 19(1), 1–17.
- Van Pelt, W. J. J., J. Oerlemans, C. H. Reijmer, R. Pettersson, V. A. Pohjola, E. Isaksson, and D. Divine (2013, June). An iterative inverse method to estimate basal topography and initialize ice flow models. *The Cryosphere* 7(3), 987–1006.
- Warburton, K. L. P., D. R. Hewitt, and J. A. Neufeld (2020, September). Tidal Grounding-Line Migration Modulated by Subglacial Hydrology. *Geophysical Research Letters* 47(17), e2020GL089088.
- Weertman, J. (1974). Stability of the Junction of an Ice Sheet and an Ice Shelf. *Journal of Glaciology* 13(67), 3–11.